PONTIFICIA UNIVERSIDAD CATOLICA DE CHILE
SCHOOL OF ENGINEERING

HYBRID DATA FIDELITY TERM APPROACH FOR QUANTITATIVE SUSCEPTIBILITY MAPPING

MATHIAS G. LAMBERT

Thesis submitted to the Office of Graduate Studies
in partial fulfillment of the requirements for the Degree of
Master of Science in Engineering

Advisors:
CRISTIÁN TEJOS

Santiago de Chile, January 2022

PONTIFICIA UNIVERSIDAD CATOLICA DE CHILE
SCHOOL OF ENGINEERING

HYBRID DATA FIDELITY TERM APPROACH FOR QUANTITATIVE SUSCEPTIBILITY MAPPING

MATHIAS G. LAMBERT

Members of the Committee:
CRISTIÁN TEJOS
SERGIO URIBE
CARLOS MILOVIC
ALEJANDRO MAC CAWLEY

Thesis submitted to the Office of Research and Graduate Studies
in partial fulfillment of the requirements for the degree of
Master of Science in Engineering

Santiago de Chile, January 2022

To my parents and my lovely Raquel

PREFACE

This thesis document presents the works performed by Mathias Lambert Villanueva during his Master of Science in Engineering. The main work (”Hybrid data fidelity term approach for Quantitative Susceptibility Mapping”) of this thesis was submitted to the journal Magnetic Resonance in Medicine in November 2021 (Manuscript #MRM-21-22642) and accepted at the ISMRM 2020 conference. Two additional works (”Non-regularized Dipole Inversion with streaking suppression via L1-norm optimization” and ”Improving Quantitative Susceptibility Mapping reconstructions via non-linear Huber loss data fidelity term”) presented at the ISMRM 2021 conference are presented in the appendices.

ACKNOWLEDGEMENTS

First I want to thank my advisor Cristián Tejos, who opened the doors to the world of research. I greatly appreciate the opportunities you have given me, the teachings you have transmitted to me, and your supervision and attention.

Thanks to all the members of the Biomedical Image Center (CIB) with whom I had the opportunity to share. Thanks to Gabriel Varela and Manuel Chapa for quickly offering me their friendship when I joined the group. An enormous thank you to Javier Silva for being an excellent friend and partner.

Special thanks to Carlos Milovic, for his friendship, for his trust, for sharing his knowledge and ideas with me. Carlos was a fundamental part of my master's degree and became a great friend and advisor for me.

I thank my parents. For providing me with an education and for their support throughout the long road we have traveled to reach this moment.

Finally, I want to thank Raquel, my girlfriend. For sharing her life with me, for her support and words of encouragement in difficult moments.

TABLE OF CONTENTS

PREFACE iv

ACKNOWLEDGEMENTS v

LIST OF FIGURES viii

LIST OF TABLES ix

ABSTRACT x

RESUMEN xii

1. INTRODUCTION 1

2. Methods 4

2.1. Hybrid data fidelity term approach for QSM (HD-QSM) 4

2.2. Experimental design 6

2.2.1. COSMOS forward simulation 6

2.2.2. 2019 QSM Challenge (RC2) - SNR1 dataset 6

2.2.3. In vivo dataset 7

3. Results 8

3.1. Cosmos Forward Simulation 8

3.2. QSM Challenge 2.0 - SNR1 dataset 8

3.3. In vivo dataset 10

4. Discussion 15

5. Conclusions 17

REFERENCES 18

APPENDIX A. SUPPLEMENTARY MATERIAL: Hybrid data fidelity term approach for QSM (HD-QSM) 26

A.1. ADMM Solver for Stage 1 26
A.2. ADMM Solver for Stage 2 28
A.3. Challenge 2.0 Experiment 30

APPENDIX B. Non-regularized Dipole Inversion with streaking suppression via L1-norm optimization 37
B.1. Title and authors 37
B.2. Synopsis 37
B.3. Abstract 37
B.3.1. Introduction 37
B.3.2. Methods 38
B.3.3. Results 39
B.3.4. Discussion & Conclusion 41
B.3.5. Acknowledgements 42

APPENDIX C. Improving Quantitative Susceptibility Mapping reconstructions via non-linear Huber loss data fidelity term (Huber-QSM) 43
C.1. Title and authors 43
C.2. Synopsis 43
C.3. Abstract 43
C.3.1. Introduction 43
C.3.2. Methods 44
C.3.3. Results 46
C.3.4. Discussion & Conclusion 46
C.3.5. Acknowledgements 47

LIST OF PUBLICATIONS, CONFERENCES AND AWARDS 50
ISI Journals 50
International Conferences 50
International Awards 50

LIST OF FIGURES

3.1 Cosmos Forward Simulation Results 11

3.2 Cosmos Forward Simulation Results 12

3.3 NRMSE evolution RC2 reconstructions 13

3.4 In-vivo reconstructions 14

A.1 RC2 Sim1 NRMSE evolution 30

A.2 RC2 Sim2 NRMSE evolution 31

A.3 Solutions at the end of stages 32

A.4 Discrepancy factor effect 33

A.5 Reconstructions without discrepancy factor 34

A.6 RC2 Sim1 reconstructions 35

A.7 RC2 Sim2 reconstructions 36

B.1 nDI-L1 COSMOS reconstructions 40

B.2 nDI-L1 RC2 SIM1SNR1 reconstructions 40

B.3 nDI-L1 in-vivo reconstructions 41

C.1 Huber loss 45

C.2 Huber-QSM COSMOS reconstructions 47

C.3 Huber-QSM COSMOS with lesions 48

C.4 Huber-QSM RC2 SIM2SNR1 reconstructions 48

C.5 Huber-QSM in-vivo reconstructions 49

LIST OF TABLES

3.1 RC2 dataset metrics 9

ABSTRACT

Susceptibility maps are usually derived from local magnetic field estimations by minimizing a functional composed of a data consistency term and a regularization term. The data consistency term measures the difference between the desired solution and the measured data using typically the L2-norm. It has been proposed to replace this L2-norm with the L1-norm, due to its robustness to outliers and reduction of streaking artifacts arising from highly noisy or strongly perturbed regions. However, in regions with high signal-to-noise ratio, the L1-norm yields a suboptimal denoising performance. In this work, we present a hybrid data fidelity approach that uses the L1-norm and subsequently the L2-norm, so that to exploit the strengths of both norms.

We developed a Hybrid Data fidelity term approach for Quantitative Susceptibility Mapping (HD-QSM) based on linear susceptibility inversion methods, with Total Variation regularization. Each functional is solved with ADMM. HD-QSM is a two-stage method that first finds a fast solution of the L1-norm functional and then uses this solution to initialize the L2-norm functional. In both norms we included spatially variable weights that improve the quality of the reconstructions.

HD-QSM produced a good quantitative reconstructions in terms of structural definition, noise reduction and avoiding streaking artifacts comparable to nonlinear methods, but with higher computational efficiency. Reconstructions performed with this method achieved first place at the lowest RMSE category in Stage 1 of the 2019 QSM Reconstruction Challenge.

The proposed method allows robust and accurate QSM reconstructions, obtaining superior performance to state-of-the-art methods.

Keywords: magnetic susceptibility, QSM, inverse problems, magnetic resonance, MRI, variational regularization, Augmented Lagrangian, L1-norm, L2-norm.

RESUMEN

Por lo general los mapas de susceptibilidad se obtienen resolviendo un problema de optimización compuesto por un término de consistencia de datos y un término regularizador. El término de consistencia de datos mide la diferencia entre la solución deseada y los datos medidos. Usualmente esta diferencia se mide utilizando la norma L2. Se ha propuesto reemplazar esta norma L2 por la norma L1, debido a su robustez frente a valores atípicos. El cambio de norma permite disminuir los artefactos originados en regiones donde la señal adquirida es muy ruidosa o está perturbada. Sin embargo, en regiones con una alta relación señal / ruido, la norma L1 produce un rendimiento subóptimo de eliminación de ruido. En este trabajo, presentamos un enfoque híbrido de consistencia de datos que utiliza la norma L1 y posteriormente la norma L2, para aprovechar las fortalezas de ambas normas.

Desarrollamos un método que utiliza un enfoque híbrido en el término de consistencia de datos (HD-QSM) basado en métodos de inversión de susceptibilidad lineal y que utiliza variación total en el término de regularización. Cada funcional se resuelve mediante la división de variables en el marco del método de multiplicadores de dirección alterna (ADMM). HD-QSM es un método de dos etapas que primero encuentra una solución rápida del funcional de la norma L1 y luego utiliza esta solución para inicializar el funcional de la norma L2. En ambas normas incluimos pesos espacialmente variables que mejoran la calidad de las reconstrucciones.

HD-QSM produjo buenas reconstrucciones en términos de definición estructural, reducción de ruido y mitigación de la generación de artefactos, comparable a los métodos no lineales, pero con menor consumo de tiempo y recursos computacionales. Con este método obtuve el primer lugar en la categoría mejor RMSE en la Etapa 1 del Desafío de Reconstrucción QSM 2019.

El método propuesto permite obtener reconstrucciones robustas y precisas, obteniendo un rendimiento superior a los métodos de QSM de última generación.

Palabras Claves: susceptibilidad magnética, QSM, problemas inversos, resonancia magnética, MRI, regularización variacional, Lagrangiano Aumentado, Norma L1, Norma L2.

1. INTRODUCTION

Quantitative Susceptibility Mapping (QSM) is an MRI reconstruction technique that allows calculating the magnetic susceptibility of tissues from the phase of gradient-echo acquisitions (E. M. Haacke et al., 2015). The magnetic susceptibility of a material is a property defined as the degree of magnetization of a material in the presence of an external magnetic field. Most biological brain tissues are intrinsically diamagnetic. Whereas diamagnetic myelin or calcium deposits are generating a magnetic field opposed to the applied field, paramagnetic materials, such as iron, react by generating a magnetic field in the same direction as that of the external field (Langkammer et al., 2012). Unlike conventional susceptibility-sensitive techniques (e.g., R2* mapping and susceptibility weighted imaging), QSM quantifies the diamagnetic and paramagnetic contributions yielding exquisite contrast between anatomical structures.

Specific physiological and pathological processes change the magnetic susceptibility and QSM can be used to quantify oxygenation levels (E. Haacke, Tang, Neelavalli, & Cheng, 2010) and detect hemorrhages and microhemorrhages (Klohs et al., 2011). Increased regional susceptibilities have been consistently found in several neurodegenerative diseases (Langkammer et al., 2012), including Alzheimer's (Acosta-Cabronero et al., 2013), Parkinson's (Acosta-Cabronero et al., 2016; Langkammer et al., 2016), Huntington's (van Bergen et al., 2016) and multiple sclerosis (Blazejewska et al., 2015; Langkammer et al., 2013).

Susceptibility maps are typically calculated by following three consecutive processing steps: phase unwrapping (Robinson et al., 2017), background field removal (Schweser, Robinson, de Rochefort, Li, & Bredies, 2017) and dipole inversion (de Rochefort, Brown, Prince, & Wang, 2008; Shmueli et al., 2009; Kressler & Rochefort, 2010; de Rochefort et al., 2010; Liu et al., 2013; Milovic, Bilgic, Zhao, Acosta-Cabronero, & Tejos, 2018; Bilgic, Chatnuntawech, Langkammer, & Setsompop, 2015; Milovic, Lambert, et al., 2021). The unwrapping stage eliminates 2π-jumps produced in the phase of the measured gradient echo signal. Background field removal eliminates the magnetic field contributions originated by

objects outside the region of interest or field of view and field inhomogeneities, leaving only the magnetization field originated from local objects. The susceptibility-to-field model considers non-interacting magnetic dipoles, each associated with a single susceptibility source. This effectively models the measured magnetic field as the convolution between a dipole kernel and the underlying susceptibility distribution (Salomir, de Senneville, & Moonen, 2003; J. Marques & Bowtell, 2005). Therefore, the susceptibility distribution might be obtained by deconvolving the local magnetic fields by the dipole kernel. This process, known as the dipole inversion, is an ill-posed inverse problem. The dipole kernel has a zero-valued biconical surface in the Fourier domain, known as the "magic cone", which impedes direct division. Truncated solutions (Shmueli et al., 2009) (i.e., replacing values below a threshold with a small number) amplify noise and contaminate the reconstructed susceptibility maps with streaking artifacts, i.e., conical patterns originated from noisy voxels.

To address this issue, the dipole inversion process is usually reformulated as an optimization problem. Optimization models minimize a functional, usually composed of two terms: a data consistency and a regularization term. The regularization term is used to include prior information about the solution, which promotes desired characteristics, e.g., smoothness or continuous solutions (Tikhonov regularizer (de Rochefort et al., 2010)) or piece-wise constant solutions (Total Variation regularizer (Chen & Cheng, 2012)). The data consistency -or data fidelity term- is a measure of the error between the proposed solution and the local magnetic fields given the susceptibility-to-field or forward model.

Commonly, the data consistency term minimizes the squared difference between the dipole-convolved solution and the local field, i.e., a squared L2-norm. The squared L2-norm is a mathematically and computationally efficient function which also defines a convex penalty function that gives a unique solution. For QSM, this approach performs relatively well with data that have been corrupted by moderate amount of noise. However, the squared L2-norm heavily penalizes large discrepancies produced by strong noise or other sources of discrepancy such as pre-processing artifacts, etc. This high penalty tends to produce susceptibility maps with streaking artifacts, especially in low SNR areas. This

behavior might be explained from a Bayesian point of view. Finding the solution that minimizes the L2-norm with noise-corrupted measured data is equivalent to finding the maximum likelihood estimate in a maximum a posteriori probability (MAP) problem, but this only happens when the noise source has a Gaussian distribution. Indeed, whereas the noise distribution in phase MRI signals with high SNR can be approximated as Gaussian, this approximation is no longer valid for low SNR (Irarrazaval, Dehghan Firoozabadi, Uribe, Tejos, & Sing-Long, 2019; Gudbjartsson & Patz, 1995).

To address this problem, Liu et al. (Liu et al., 2013) proposed a nonlinear data fidelity term that computes the error of the forward model at the complex image domain improving robustness to noise at the expense of higher computational cost. Later, Milovic et al. (Milovic, Lambert, et al., 2021) proposed to use an L1-norm data consistency term (least absolute error minimization), producing a better performance against outlier voxels (Boyd, Parikh, Chu, Peleato, & Eckstein, 2011; Li & Swetits, 1998; "Asymptotic Theory of Least Absolute Error Regression", 1978; Wang, 2013). Compared with the L2-norm, the L1-norm penalizes large discrepancies between the proposed solution and the measured data less severely. This prevents energy-spilling from voxels with large discrepancies with respect to their neighbors, which in turn reduces the generation and propagation of streaking artifacts. However, from a Bayesian point of view, the L1-norm does not have similar denoising capabilities as the L2-norm, thus the resulting images have a residual noise component and lower SNR (Milovic, Lambert, et al., 2021).

In this thesis we present a Hybrid Data fidelity term approach for Quantitative Susceptibility Mapping (HD-QSM). This dipole inversion algorithm sequentially uses linear L1- and L2-norms for data consistency. The resulting algorithm successfully combines the strengths of both norms. HD-QSM participated at the 2019 QSM Reconstruction Challenge (RC2 - Seoul, Korea) (Committee et al., 2021; J. P. Marques et al., 2021), obtaining the first place at the lowest RMSE category in Stage 1. We here present a validation of our method using simulations and in-vivo data, and exhaustive comparisons with previous methods.

2. METHODS

2.1. Hybrid data fidelity term approach for QSM (HD-QSM)

The proposed method HD-QSM consists of two stages. The first stage finds a suitable initial solution that is robust to streaking artifacts (Milovic, Lambert, et al., 2021). For this purpose, we use the following linear optimization problem:

$$\arg\min_{\chi_1} \left\| w \cdot \left(F^H D F \chi_1 - \phi \right) \right\|_1 + \lambda_1^{L_1} \cdot \left\| \nabla \chi_1 \right\|_1 \tag{2.1}$$

where $\|\cdot\|_1$ is the L1-norm, F is the Fourier transform with its inverse F^H, $D = \gamma H_0 TE \left(\frac{1}{3} - \frac{k_z^2}{k^2} \right)$ is the dipole kernel, ϕ is the local phase map, χ_1 is the susceptibility distribution obtained in this first stage, $\|\nabla \chi_1\|_1$ is the total variation regularizer, and $\lambda_1^{L_1}$ is the regularization weight used in this first stage. w is a ROI binary mask or a magnitude-based weight defined as

$$w = \frac{\sum_{i=1}^{N} \text{Magn}_i^2 \cdot \text{TE}_i}{\sum_{i=1}^{N} \text{Magn}_i \cdot \text{TE}_i} \tag{2.2}$$

where N is the number of echoes, Magn_i is the magnitude of echo i, and TE_i is the i-*th* echo time.

The second stage is to solve the following linear functional using the solution of the previous stage (χ_1) as the initialization.

$$\arg\min_{\chi_2} \frac{1}{2} \left\| \mathbb{W} \cdot \left(F^H D F \chi_2 - \phi \right) \right\|_2^2 + \lambda_1^{L_2} \left\| \nabla \chi_2 \right\|_1 \tag{2.3}$$

where $\|\cdot\|_2^2$ is the L2-norm, $\mathbb{W}$ is a spatially variable weight modulated by the voxel-wise phase discrepancy factor between the solution obtained in the first stage (convolved by the dipole kernel) and the acquired local phase:

$$\mathbb{W} = w \cdot \left(1 - \frac{\left| \phi - F^H D F \chi_1 \right|}{\max\left(\left| \phi - F^H D F \chi_1 \right| \right)} \right) \tag{2.4}$$

The discrepancy factor prevents the propagation of streaking artifacts by enforcing the data consistency term to penalize areas with low SNR and areas contaminated with phase inconsistencies less heavily.

The functionals were solved using the ADMM framework (Bilgic et al., 2015) as described for FANSI (Milovic et al., 2018) and L1-QSM (Milovic, Lambert, et al., 2021). A straightforward implementation would require to fine tune six parameters: two regularization weights $\left(\lambda_1^{L_1},\, \lambda_1^{L_2}\right)$, and four Lagrangian weights derived from the ADMM solver associated with gradient consistency weights $\left(\mu_1^{L_1},\, \mu_1^{L_2}\right)$ and data fidelity consistency weights $\left(\mu_2^{L_1},\, \mu_2^{L_2}\right)$. These Lagrangian weights are introduced by the variable splitting procedure of ADMM, as described in the Appendix A. As in most optimization based QSM algorithms, parameters must be set using some heuristics (Milovic, Prieto, et al., 2021) (e.g., L-curve approach (Hansen, 2000)). To simplify the parameter-tuning process, we propose the following heuristic, derived from the numerical relationship between the L1- and L2-norms: $\lambda_1^{L_1} = \sqrt{\lambda_1^{L_2}}$, $\mu_1^{L_1} = \sqrt{\mu_1^{L_2}}$, $\mu_2^{L_1} = \mu_2^{L_2} = 1$. Considering also the heuristic proposed for FANSI (Milovic et al., 2018) $10 \leq \frac{\mu_1}{\lambda_1} \leq 100$, where values within the range do not produce major variations on the optimal reconstruction. We therefore simplify the parameter setting problem to a one free parameter, $\lambda_1^{L_2}$.

The numbers of iterations in each stage $(i_1,\, i_2)$ can be considered as free parameters to be tuned. However, as shown in our experiments, these are not sensitive parameters and might be fixed a priori. Considering a total number of iterations N we recommend $i_1 \in [10,\, 100]$ and $i_2 = N - i_1$. For the Reconstruction Challenge 2.0 (Committee et al., 2021), our winning reconstructions used this heuristic with the following parameters $i_1 = 20$, $i_2 = 280$, $\lambda_1^{L_2} = 6.3096 \times 10^{-6}$ and $\frac{\mu_1}{\lambda_1} = 10$.

HD-QSM was compared with linear and non-linear QSM methods using total variation as regularizer. For convenience, we will use the following nomenclature. L1 and nlL1 correspond to the linear and non-linear L1-norm methods proposed in L1-QSM (Milovic, Lambert, et al., 2021), respectively. L2 and nlL2 correspond to the linear and non-linear L2-norm methods proposed in FANSI (Milovic et al., 2018), respectively. L1L2 corresponds

to the HD-QSM method with the proposed heuristic and L1L2wH corresponds to the HD-QSM without the heuristic (i.e., optimizing each parameter independently). Comparisons were performed using synthetic data and in vivo acquisitions, as described below.

2.2. Experimental design

2.2.1. COSMOS forward simulation

We used the COSMOS (Liu, Spincemaille, De Rochefort, Kressler, & Wang, 2009) reconstruction included in the 2016 QSM Reconstruction Challenge (RC1) (Langkammer et al., 2018) dataset as ground truth. We forward-simulated the phase and added complex Gaussian noise with SNR 40, 100 and 300. Additionally, we forward-simulated the phase (SNR=100) with two consecutive phase jumps $(\pm 20\pi)$ to generate strong phase inconsistencies. These phase simulations were used as input for the QSM reconstructions of L1, L2 and L1L2 methods to compare their performances. Optimal reconstructions were obtained for each method by optimizing the normalized root mean squares error (NRMSE). We performed an sensitivity analysis evaluating the quality of the reconstructions around the optimal regularization parameter (λ^*), within a range defined by $[0.1 \cdot \lambda^*,\ 10 \cdot \lambda^*]$, sampled at $\lambda_i = \lambda^* \cdot 10^{\frac{i}{30}}$, with $i \in [-30,\ -29,\ \ldots,\ 29,\ 30]$.

2.2.2. 2019 QSM Challenge (RC2) - SNR1 dataset

In the context of the RC2 (Committee et al., 2021), two simulated datasets (J. P. Marques et al., 2021) with different SNRs were provided. Each dataset consisted of two brain images: Sim1 and Sim2. Sim2 had higher contrast between white matter and gray matter than Sim1. Additionally, a strong calcification was included in Sim2. We used the SNR1 dataset, as it presents a lower SNR ratio (SNR1=100 vs. SNR2 = 1000). We estimated the local magnetic field from the phase of the simulated multi-echo acquisitions using a magnitude-weighted least-squares fitting. Field maps were zero-padded to 256x256x256 to prevent large scale aliasing and other artifacts. All reconstructions were stopped when they reached 300 iterations, and the reconstruction parameters were set to minimize NRMSE. For each of the optimal NRMSE reconstructions, we computed the error metrics used in

RC2, namely (Committee et al., 2021): dNRMSE, dNRMSE TISSUE, dNRMSE DeepGM, dNRMSE blood, Calcification streaking and Deviation from calcification moment. We considered two additional global metrics: Susceptibility-tuned Structural Similarity Index Metric (XSIM) (Milovic, Tejos, & Irarrazaval, 2019) and the High Frequency Error Norm (HFEN) (Ravishankar & Bresler, 2011).

2.2.3. In vivo dataset

We performed an in vivo acquisition on a Siemens 3T scanner (Magnetom Trio Tim; Siemens Healthcare, Erlangen, Germany) with a 12-channel phased-array head coil. We used a GRE sequence with six echoes of a patient showing extensive brain hemorrhage with the following sequence parameters: TE1=4.92ms, ΔTE=4.92ms, TR=35ms, flip angle=15°, 232×288×64 matrix with 0.8×0.8×2mm^3 voxel size, and T_{acq}=4:51 min. Phase unwrapping was performed with SEGUE (Karsa & Shmueli, 2019) and background field removal was performed by Projection onto Dipole Fields (Liu et al., 2011). We estimated the local field using a magnitude-weighted least-squares phase fitting. Background field residuals were removed using the harmonic phase estimation obtained with the Weak-harmonic QSM method (WH-TV) (Milovic, Bilgic, et al., 2019).

3. RESULTS

3.1. Cosmos Forward Simulation

L1L2 obtained the best performance for medium and low SNRs (Figures 3.1.A and 3.1.B), whereas L1 achieved the best results for high SNR (Figure 3.1.C). Independently of the SNR level, L1L2 obtained the most stable performance, i.e., varying the regularization parameter around the optimum produced the smallest NRMSE change.

While L2 reconstructions yielded streaking artifacts in the presence of phase inconsistencies, both L1 and L1L2 could successfully suppress those artifacts (Figure 3.2). To compensate the generation of streaking artifacts, the minimization of the NRMSE produced an over-regularized L2 reconstruction. L1L2 reconstructions demonstrated better delineation or definition (without over-regularization) of small blood vessels along with better contrast between white and gray matter.

3.2. QSM Challenge 2.0 - SNR1 dataset

HD-QSM (L1L2 and L1L2wH) achieved the best performance in most of the analyzed metrics, especially when considering RMSE-based metrics (Table 3.1). The metrics obtained using the proposed heuristic (L1L2) are similar as those obtained by tuning all parameters (L1L2wH). nlL1 obtains the second-best performance in NRMSE (optimized variable), but the processing time is more than two times larger than those of the linear competitors.

The optimal number of L1 iterations (i_1) was 40 and 280 for L1L2 and L1L2wH, respectively. For different i_1, the optimized reconstructions of L1L2 and L1L2wH showed differences less than 1% in NRMSE (Figures A.1-A.5).

The reconstructions obtained for each method are presented in figures A.6 and A.7. Figure 3.3 shows the evolution of NRMSE per iteration of the optimal reconstructions

TABLE 3.1. Metrics of RMSE based optimal reconstructions. We evaluated the QSM challenge 2.0 metrics plus XSIM, HFEN and computation time. In simulation 1 L1L2 and L1L2wH scored highest in 6 out of 7 metrics evaluated. In simulation 2 L1L2wH scored best in 6 out of 9 metrics. L1L2wH is slightly superior to L1L2, removing L1L2wH from the comparison the best performance is obtained by L1L2.

	Sim1					
	L1L2wH	L1L2	L1	L2	nlL1	nlL2
RMSE	29,4	30,0	31,8	30,7	30,4	30,7
dRMSE	30,9	30,7	31,8	32,6	31,8	32,6
dRMSE Tissue	39,3	39,0	38,7	41,6	41,0	41,6
dRMSE Blood	39,7	39,6	44,3	42,0	41,3	42,0
dRMSE DGM	17,5	17,6	18,4	17,9	17,8	17,9
XSIM	0,955	0,950	0,950	0,946	0,929	0,946
HFEN	28,3	28,0	29,3	29,5	29,1	29,5
Time (s)	789	777	781	865	2022	962
λL1 (Reg. Weight)	5,6E-03	2,7E-03	1,3E-02	-	2,8E-04	-
λL2 (Reg. Weight)	7,5E-06	7,3E-06	-	7,9E-06	-	8,0E-06
	Sim2					
	L1L2wH	L1L2	L1	L2	nlL1	nlL2
RMSE	28,7	29,1	30,1	30,4	29,4	30,4
dRMSE	30,4	30,9	31,0	33,5	31,3	33,5
dRMSE Tissue	29,4	30,2	29,2	32,8	30,5	32,8
dRMSE Blood	59,9	60,2	63,3	63,5	61,2	63,5
dRMSE DGM	20,8	21,3	20,9	21,7	21,0	21,7
CalcStreak	0,037	0,038	0,040	0,045	0,038	0,045
CalcError	15,5	15,6	15,4	16,9	16,4	16,9
XSIM	0,945	0,934	0,946	0,939	0,875	0,939
HFEN	29,5	29,7	29,5	31,4	30,3	31,4
Time (s)	773	776	808	880	2051	966
λL1 (Reg. Weight)	5,6E-03	2,6E-03	1,2E-02	-	2,5E-04	-
λL2 (Reg. Weight)	7,0E-06	6,8E-06	-	8,3E-06	-	8,4E-06

achieved for each method. The curves for L2 and nlL2 are overlapped since their performances were almost identical. Stage 1 of L1L2 and L1L2wH diverged before the transition to stage 2 and then it quickly converged again.

The optimal regularization values of our proposed methods (L1L2 and L1L2wH) were smaller than those respectively obtained for L1 and L2 methods (Table 3.1). Having a

smaller $\lambda_1^{L_1}$, might explain the divergence observed in NRMSE curves in our stage 1. Figures A.4 and A.5 present reconstructions at the end of stage 1 and stage 2, with and without the use of the weight modulated by the voxel-wise phase discrepancy factor. The use of the discrepancy factor helps the L2-norm to reduce the artifacts present in the image provided by stage 1. This is done penalizing with a low weight those voxels that might produce strong artifacts.

3.3. In vivo dataset

Figure 3.4 presents the in-vivo reconstructions for each method. The optimal reconstructions were chosen by visual inspection around the optimum indicated by the L-curve analysis. The reconstruction of the linear L1-norm method shows a hallucinated suppression of the frontal lesion which limits the clinical useability of this method. All other methods were able to successfully recover the lesions, with L1L2 showing the fewest shadow artifacts adjacent to the frontal and posterior lesions.

The difference maps highlight that the L1L2 reconstruction is smooth like the L2-norm reconstructions but comes with a better structural definition such as the nlL1 reconstruction. L1L2 and nlL1 resolved structural details such as the posterior lesion generating only minor shadows around it.

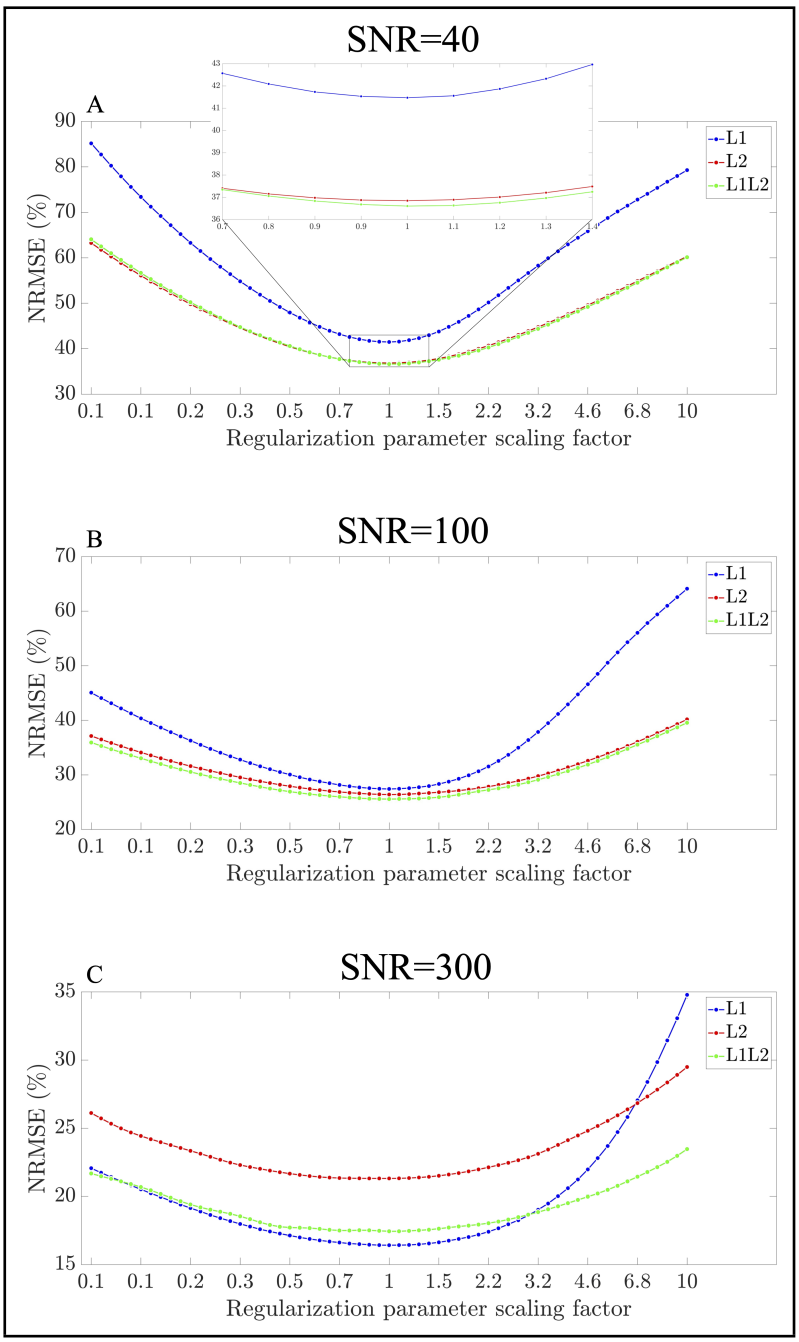

FIGURE 3.1. Subfigures A, B and C show the RMSE for different regularization parameters normalizing the scale with center at the optimum.

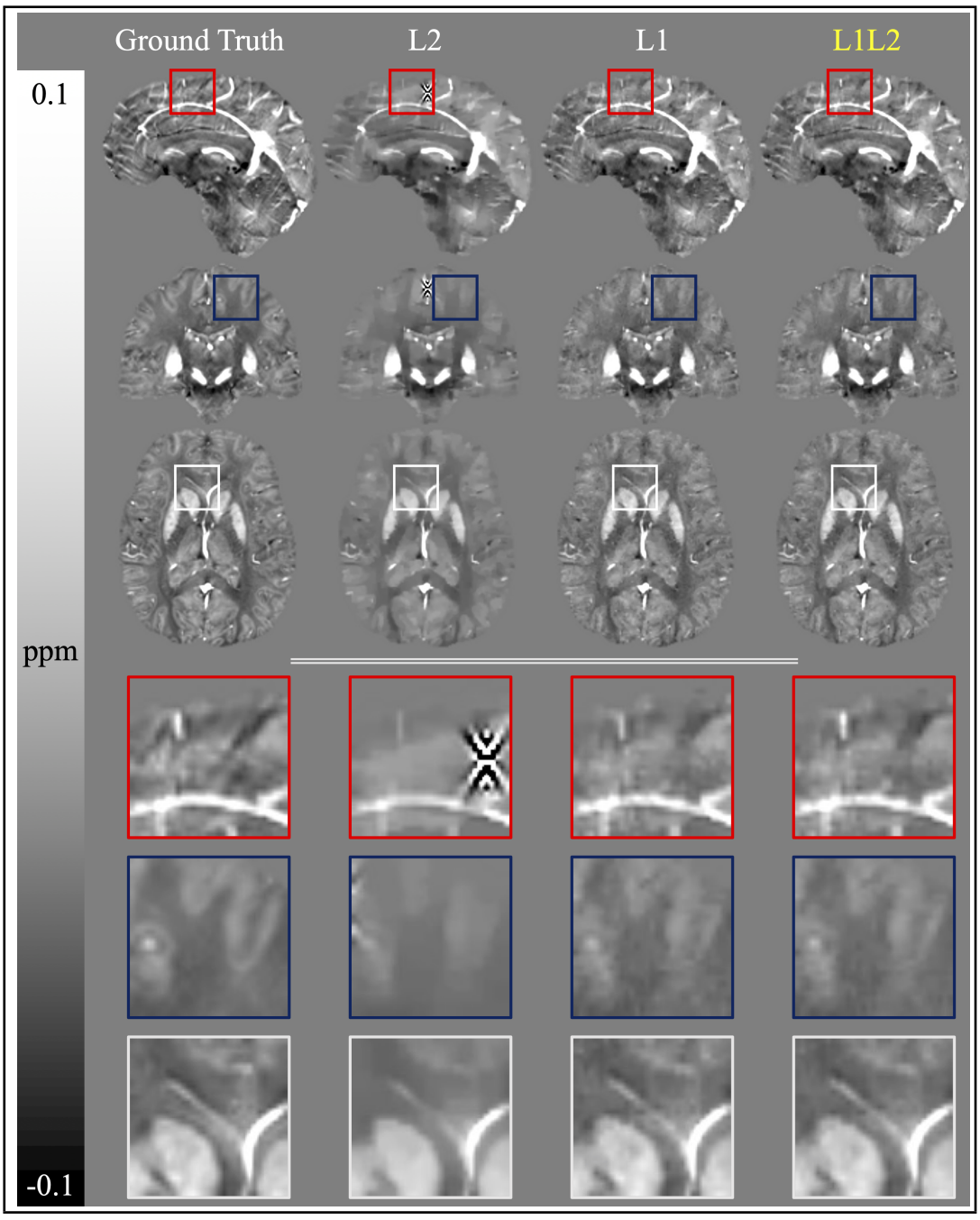

FIGURE 3.2. Optimal reconstructions of L1, L2 and L1L2 over the simulation with SNR=100 and phase jumps. Areas of interest are enclosed in bounding boxes and magnified to show details.

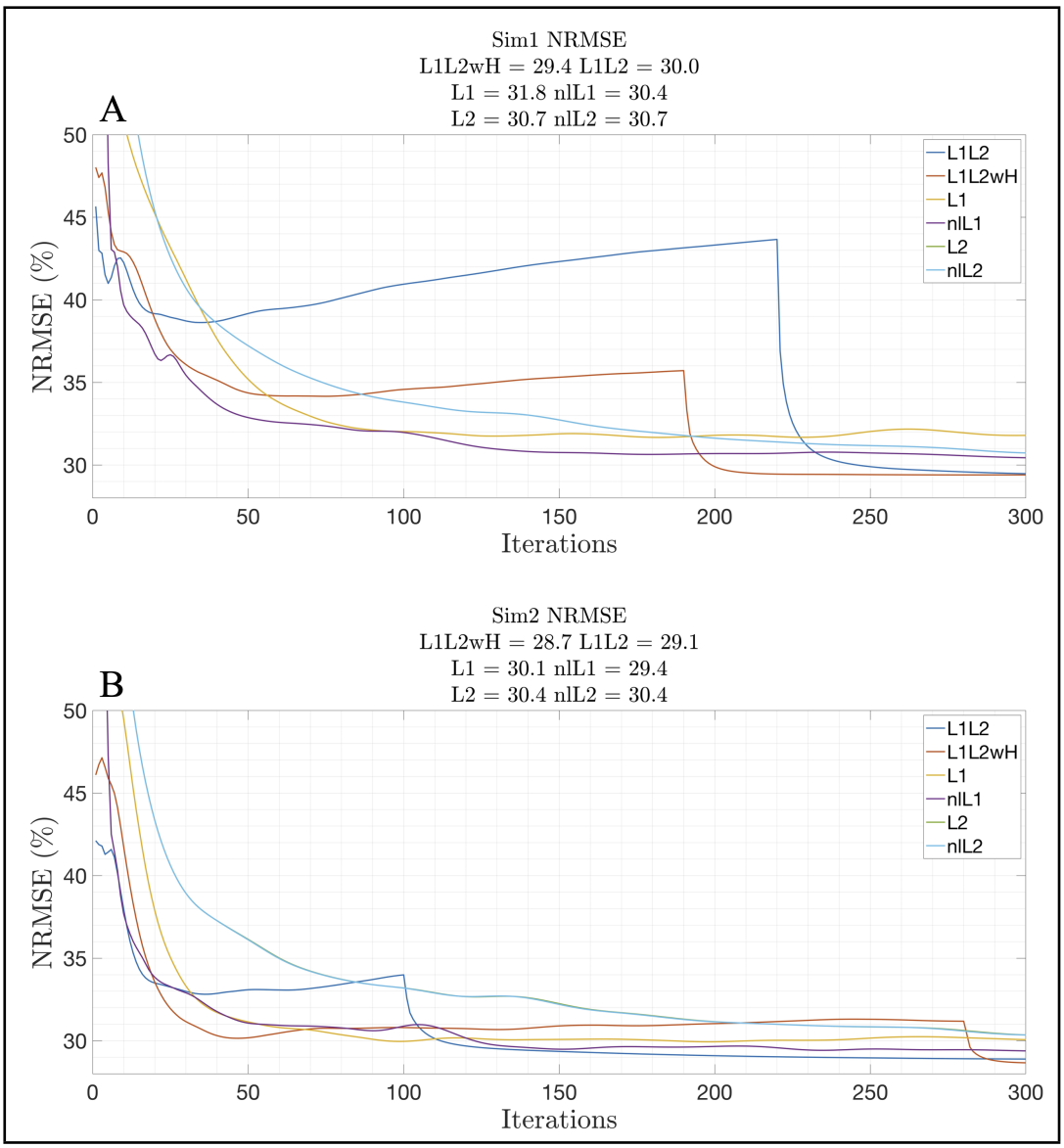

FIGURE 3.3. Evolution of NRMSE by iterations for all methods on Sim1 and Sim2. The curves of L2 and nlL2 overlap. The first stage of L1L2 and L1L2wH diverges while stage 2 converges fast. The difference in NRMSE between L1L2 and L1L2wH is 0.5 points.

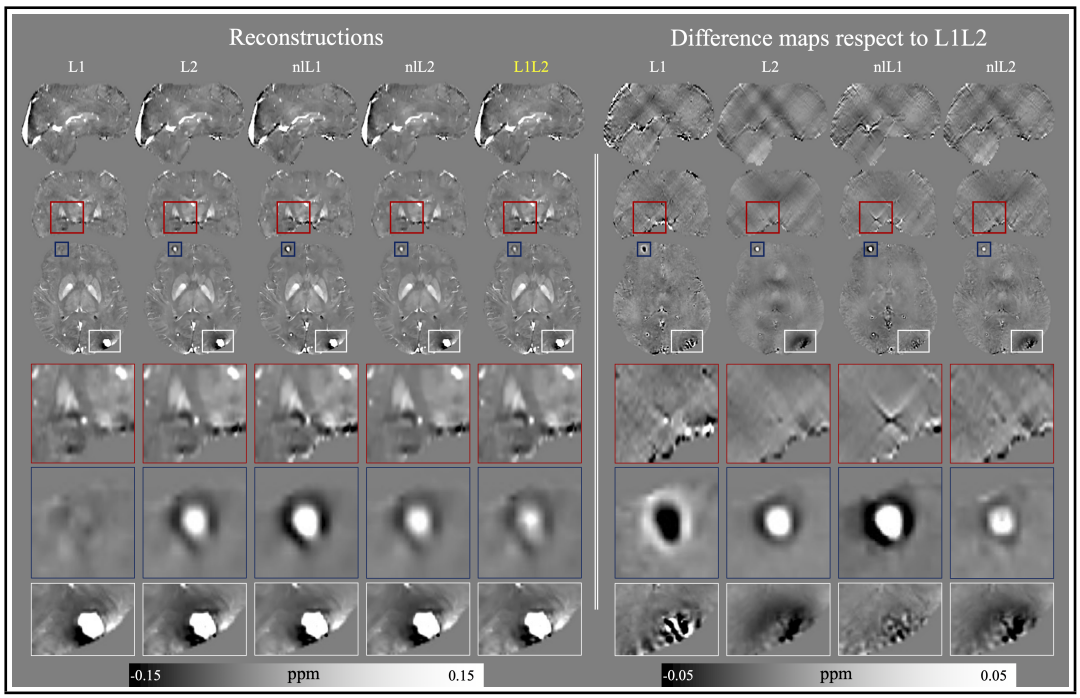

FIGURE 3.4. Optimal reconstructions obtained by visual inspection around the optimum indicated by the L-curve analysis. Areas of interest are enclosed in bounding boxes. The red box shows the basal ganglia region and encloses a zone with a hyper-intense structure (might be a blood vessel shown as a white circle) in the center. nlL1 generates an artifact in the structure, generating a different geometry and propagating a streaking artifact. The blue and white boxes enclose frontal and posterior lesions respectively. L1L2 generates reconstructions with less artifacts around the lesions.

4. DISCUSSION

HD-QSM is an iterative method that differs from current methods as it is composed of two consecutive stages using the L1 and L2 norm in a linear data consistency term. HD-QSM provides good reconstructions at low, medium and high SNRs, and obtains superior performances at low and medium SNRs compared to single-stage linear methods using the L1 norm, or alternatively, the L2 norm. The use of two stages allows HD-QSM to exploit the strengths of both norms, the reconstructions are robust to outliers, providing good noise reduction capabilities and stability with respect to the regularization parameter.

The data consistency weights (Eqs. 2.2 and 2.4) play a fundamental role in HD-QSM. They help to identify voxels that generate artifacts so that the L2-norm data consistency penalizes them less heavily and avoids generating artifacts. It also allows stage 1 to search for a sub-regularized solution rich in structural information and provides stage 2 with an initial solution closer to the optimum. This makes HD-QSM regularization parameters lower than their single-stage counterparts.

Our method has 6 free parameters to be tuned. However, we propose a heuristic to reduce this complexity to only one free parameter. After a fixed total number of iterations, the difference of the NRMSE obtained between the six free parameter method and the proposed heuristic was always less than 1%, independent of the distribution of iterations between the first and the second step. Even though, the L1 minimization step seems to diverge after a few iterations, the L2 stage plus the use of data consistency weights can rapidly reduce the errors. In other words, setting only one free parameter and running only a few iterations for the L1 minimization step would be enough to define a good initialization for the L2 minimization step, and lately, achieve high quality QSM reconstructions.

In terms of image quality, the proposed two-stage solver represents an improvement over linear and non-linear formulations in terms of reducing noise and preventing streaking artifacts emanating from low SNR regions. Compared to L2-norm methods, HD-QSM produced reconstructions with better structural definition and better artifact management.

Compared to L1-norm methods, HD-QSM produced reconstructions with a less noisy visual appearance and closer to the ground truth. HD-QSM requires similar computational time compared to linear methods and outperforms non-linear methods.

The idea of solving QSM reconstructions using a previous reconstruction as a starting point might be extended to single-step formulations, i.e., including phase unwrapping and background field removal into the functionals. Initialization based on solutions that do not require parameter tuning can also be explored (i.e., non-regularized functional, deep learning models), in which case this model would serve as a refinement step.

5. CONCLUSIONS

HD-QSM combines the beneficial features of the L1- and L2-norms to obtain high quality QSM reconstructions, namely: good structural definition, noise reduction and preventing streaking artifacts, while maintaining the computational complexity of a linear method. We also proposed a simple and effective heuristic that reduces fine-tuning to only one parameter to achieve optimal performance. HD-QSM demonstrated exquisite numerical performance in the QSM challenge 2.0 and in pathological MRI datasets with structural abnormalities and conspicuous features.

REFERENCES

Acosta-Cabronero, J., Cardenas-Blanco, A., Betts, M. J., Butryn, M., Valdes-Herrera, J. P., Galazky, I., & Nestor, P. J. (2016, 11). The whole-brain pattern of magnetic susceptibility perturbations in Parkinson's disease. *Brain*, *140*(1), 118-131. doi: 10 .1093/brain/aww278

Acosta-Cabronero, J., Williams, G. B., Cardenas-Blanco, A., Arnold, R. J., Lupson, V., & Nestor, P. J. (2013). In vivo quantitative susceptibility mapping (QSM) in Alzheimer's disease. *PLoS ONE*, *8*(11). doi: 10.1371/journal.pone.0081093

Asymptotic theory of least absolute error regression. (1978). *Journal of the American Statistical Association*, *73*(363), 618–622.

Bilgic, B., Chatnuntawech, I., Langkammer, C., & Setsompop, K. (2015). Sparse methods for quantitative susceptibility mapping. *Wavelets and Sparsity XVI, SPIE 2015*. doi: 10.1117/12.2188535

Blazejewska, A. I., Al-Radaideh, A. M., Wharton, S., Lim, S. Y., Bowtell, R. W., Constantinescu, C. S., & Gowland, P. A. (2015). Increase in the iron content of the substantia nigra and red nucleus in multiple sclerosis and clinically isolated syndrome: A 7 tesla mri study. *Journal of Magnetic Resonance Imaging*, *41*(4), 1065-1070. doi: https://doi.org/10.1002/jmri.24644

Boyd, S., Parikh, N., Chu, E., Peleato, B., & Eckstein, J. (2011). Distributed optimization and statistical learning via the alternating direction method of multipliers. *Foundations and Trends in Machine Learning*, *3*(1), 1-122. doi: 10.1561/ 2200000016

Chen, D. Q., & Cheng, L. Z. (2012). Spatially adapted total variation model to remove multiplicative noise. *IEEE Transactions on Image Processing*, *21*(4), 1650-1662. doi: 10.1109/TIP.2011.2172801

Committee, Q. C. . O., Bilgic, B., Langkammer, C., Marques, J. P., Meineke, J., Milovic, C., & Schweser, F. (2021). Qsm reconstruction challenge 2.0: Design and report of results. *Magnetic Resonance in Medicine*, *86*(3), 1241-1255. doi: https://doi.org/10.1002/mrm.28754

de Rochefort, L., Brown, R., Prince, M. R., & Wang, Y. (2008). Quantitative mr susceptibility mapping using piece-wise constant regularized inversion of the magnetic field. *Magnetic Resonance in Medicine*, *60*(4), 1003-1009. doi: https://doi.org/10.1002/mrm.21710

de Rochefort, L., Liu, T., Kressler, B., Liu, J., Spincemaille, P., Lebon, V., ... Wang, Y. (2010, January). Quantitative susceptibility map reconstruction from MR phase data using bayesian regularization: validation and application to brain imaging. *Magnetic resonance in medicine : official journal of the Society of Magnetic Resonance in Medicine / Society of Magnetic Resonance in Medicine*, *63*(1), 194–206. doi: 10.1002/mrm.22187

Gudbjartsson, H., & Patz, S. (1995). The Rician distribution of noisy MRI data. *Magnetic Resonance in Medicine*, *34*(6), 910–914. doi: 10.1002/mrm.1910340618

Haacke, E., Tang, J., Neelavalli, J., & Cheng, Y. (2010). Susceptibility mapping as a means to visualize veins and quantify oxygen saturation. *Journal of Magnetic Resonance Imaging*, *32*(3), 663-676. doi: https://doi.org/10.1002/jmri.22276

Haacke, E. M., Liu, S., Buch, S., Zheng, W., Wu, D., & Ye, Y. (2015). Quantitative susceptibility mapping: current status and future directions. *Magnetic Resonance Imaging*, *33*(1), 1 - 25. doi: https://doi.org/10.1016/j.mri.2014.09.004

Hansen, P. C. (2000). The l-curve and its use in the numerical treatment of inverse problems. In *in computational inverse problems in electrocardiology, ed. p. johnston, advances in computational bioengineering* (pp. 119–142). WIT Press.

Huber, P. J. (1964). Robust Estimation of a Location Parameter. *The Annals of Mathematical Statistics*, *35*(1), 73 – 101. doi: 10.1214/aoms/1177703732

Irarrazaval, P., Dehghan Firoozabadi, A., Uribe, S., Tejos, C., & Sing-Long, C. (2019). Noise estimation for the velocity in mri phase-contrast. *Magnetic Resonance Imaging*, *63*, 250-257. doi: https://doi.org/10.1016/j.mri.2019.08.028

Karsa, A., & Shmueli, K. (2019). Segue: A speedy region-growing algorithm for unwrapping estimated phase. *IEEE Transactions on Medical Imaging*, *38*(6), 1347-1357. doi: 10.1109/TMI.2018.2884093

Klohs, J., Deistung, A., Schweser, F., Grandjean, J., Dominietto, M., Waschkies, C., ... Rudin, M. (2011). Detection of cerebral microbleeds with quantitative susceptibility mapping in the arcabeta mouse model of cerebral amyloidosis. *Journal of Cerebral Blood Flow & Metabolism*, *31*(12), 2282-2292. doi: 10.1038/jcbfm.2011.118

Kressler, B., & Rochefort, L. D. (2010). Nonlinear regularization for per voxel estimation of magnetic susceptibility distributions from MRI field maps. *Medical Imaging, ...*, *29*(2), 273–281.

Langkammer, C., Liu, T., Khalil, M., Enzinger, C., Jehna, M., Fuchs, S., ... Ropele, S. (2013). Quantitative susceptibility mapping in multiple sclerosis. *Radiology*, *267*(2), 551-559. (PMID: 23315661) doi: 10.1148/radiol.12120707

Langkammer, C., Pirpamer, L., Seiler, S., Deistung, A., Schweser, F., Franthal, S., ... Schwingenschuh, P. (2016, 09). Quantitative susceptibility mapping in parkinson's disease. *PLOS ONE*, *11*(9), 1-13. doi: 10.1371/journal.pone.0162460

Langkammer, C., Schweser, F., Krebs, N., Deistung, A., Goessler, W., Scheurer, E., ... Reichenbach, J. R. (2012). Quantitative susceptibility mapping (QSM) as a means to measure brain iron? A post mortem validation study. *NeuroImage*, *62*(3), 1593–1599. doi: 10.1016/j.neuroimage.2012.05.049

Langkammer, C., Schweser, F., Shmueli, K., Kames, C., Li, X., Guo, L., ... Bilgic, B. (2018). Quantitative susceptibility mapping: Report from the 2016 reconstruction challenge. *Magnetic Resonance in Medicine*, *79*(3), 1661–1673. doi: 10.1002/mrm.26830

Li, W., & Swetits, J. J. (1998). The linear l1 estimator and the huber m-estimator. *SIAM Journal on Optimization*, *8*(2), 457-475. doi: 10.1137/S1052623495293160

Li, W., Wu, B., & Liu, C. (2011, April). Quantitative susceptibility mapping of human brain reflects spatial variation in tissue composition. *NeuroImage*, *55*(4), 1645–56. doi: 10.1016/j.neuroimage.2010.11.088

Liu, T., Khalidov, I., de Rochefort, L., Spincemaille, P., Liu, J., Tsiouris, A. J., & Wang, Y. (2011). A novel background field removal method for mri using projection onto dipole fields (pdf). *NMR in Biomedicine*, *24*(9), 1129–1136. doi: 10.1002/nbm.1670

Liu, T., Spincemaille, P., De Rochefort, L., Kressler, B., & Wang, Y. (2009). Calculation of susceptibility through multiple orientation sampling (COSMOS): A method for conditioning the inverse problem from measured magnetic field map to susceptibility source image in MRI. *Magnetic Resonance in Medicine*, *61*(1), 196–204. doi: 10.1002/mrm.21828

Liu, T., Wisnieff, C., Lou, M., Chen, W., Spincemaille, P., & Wang, Y. (2013). Nonlinear formulation of the magnetic field to source relationship for robust quantitative susceptibility mapping. *Magnetic Resonance in Medicine*, *69*(2), 467–476. doi: 10.1002/mrm.24272

Marques, J., & Bowtell, R. (2005, April). Application of a Fourier-based method for rapid calculation of field inhomogeneity due to spatial variation of magnetic susceptibility. *Concepts in Magnetic Resonance Part B: Magnetic Resonance Engineering*, *25B*(1), 65–78. doi: 10.1002/cmr.b.20034

Marques, J. P., Meineke, J., Milovic, C., Bilgic, B., Chan, K.-S., Hedouin, R., ... Schweser, F. (2021). Qsm reconstruction challenge 2.0: A realistic in silico head phantom for mri data simulation and evaluation of susceptibility mapping procedures. *Magnetic Resonance in Medicine*, *86*(1), 526-542. doi: https://doi.org/10.1002/mrm.28716

Milovic, C., Bilgic, B., Zhao, B., Acosta-Cabronero, J., & Tejos, C. (2018). Fast nonlinear susceptibility inversion with variational regularization. *Magnetic Resonance in Medicine*, *80*(2), 814-821. doi: https://doi.org/10.1002/mrm.27073

Milovic, C., Bilgic, B., Zhao, B., Langkammer, C., Tejos, C., & Acosta-Cabronero, J. (2019). Weak-harmonic regularization for quantitative susceptibility mapping. *Magnetic Resonance in Medicine*, *81*(2), 1399-1411. doi: https://doi.org/10.1002/mrm.27483

Milovic, C., Lambert, M., Langkammer, C., Bredies, K., Irarrazaval, P., & Tejos, C. (2021). Streaking artifact suppression of quantitative susceptibility mapping reconstructions via l1-norm data fidelity optimization (l1-qsm). *Magnetic Resonance in Medicine*, *n/a*(n/a). doi: https://doi.org/10.1002/mrm.28957

Milovic, C., Prieto, C., Bilgic, B., Uribe, S., Acosta-Cabronero, J., Irarrazaval, P., & Tejos, C. (2021). Comparison of parameter optimization methods for quantitative susceptibility mapping. *Magnetic Resonance in Medicine*, *85*(1), 480-494. doi: https://doi.org/10.1002/mrm.28435

Milovic, C., Tejos, C., & Irarrazaval, P. (2019). Structural similarity index metric setup for qsm applications (xsim). 5th International Workshop on MRI Phase Contrast Quantitative Susceptibility Mapping, Seoul, Korea.

Polak, D., Chatnuntawech, I., Yoon, J., Iyer, S. S., Milovic, C., Lee, J., ... Bilgic, B. (2020). Nonlinear dipole inversion (ndi) enables robust quantitative susceptibility mapping (qsm). *NMR in Biomedicine*, *33*(12), e4271. (e4271 NBM-19-0164.R2) doi: https://doi.org/10.1002/nbm.4271

Ravishankar, S., & Bresler, Y. (2011). Mr image reconstruction from highly undersampled k-space data by dictionary learning. *IEEE Transactions on Medical Imaging*, *30*(5), 1028-1041. doi: 10.1109/TMI.2010.2090538

Robinson, S. D., Bredies, K., Khabipova, D., Dymerska, B., Marques, J. P., & Schweser, F. (2017). An illustrated comparison of processing methods for mr phase imaging and qsm: combining array coil signals and phase unwrapping. *NMR in Biomedicine*, *30*(4), e3601–n/a. (e3601 NBM-15-0313.R2) doi: 10.1002/nbm.3601

Salomir, R., de Senneville, B. D., & Moonen, C. T. (2003, October). A fast calculation method for magnetic field inhomogeneity due to an arbitrary distribution of bulk susceptibility. *Concepts in Magnetic Resonance*, *19B*(1), 26–34. doi: 10.1002/cmr.b.10083

Schweser, F., Robinson, S. D., de Rochefort, L., Li, W., & Bredies, K. (2017). An illustrated comparison of processing methods for phase mri and qsm: removal of background field contributions from sources outside the region of interest. *NMR in Biomedicine*, *30*(4), e3604–n/a. (e3604 NBM-15-0314.R2) doi: 10.1002/nbm.3604

Shmueli, K., de Zwart, J. a., van Gelderen, P., Li, T.-Q., Dodd, S. J., & Duyn, J. H. (2009, December). Magnetic susceptibility mapping of brain tissue in vivo using MRI phase data. *Magnetic resonance in medicine : official journal of the Society*

of Magnetic Resonance in Medicine / Society of Magnetic Resonance in Medicine, *62*(6), 1510–22. doi: 10.1002/mrm.22135

van Bergen, J., Hua, J., Unschuld, P., Lim, I., Jones, C., Margolis, R., ... Li, X. (2016). Quantitative susceptibility mapping suggests altered brain iron in premanifest huntington disease. *American Journal of Neuroradiology*, *37*(5), 789–796. doi: 10 .3174/ajnr.A4617

Wang, L. (2013). The l1 penalized lad estimator for high dimensional linear regression. *Journal of Multivariate Analysis*, *120*, 135-151. doi: https://doi.org/10.1016/j.jmva.2013.04.001

Zhou, D., Liu, T., Spincemaille, P., & Wang, Y. (2014). Background field removal by solving the laplacian boundary value problem. *NMR in Biomedicine*, *27*(3), 312–319. (NBM-13-0115.R3) doi: 10.1002/nbm.3064

Appendix

APPENDIX A. SUPPLEMENTARY MATERIAL: HYBRID DATA FIDELITY TERM APPROACH FOR QSM (HD-QSM)

A.1. ADMM Solver for Stage 1

The first stage of HD-QSM is to solve the following linear QSM functional with L1-norm:

$$\arg\min_{\chi_1} \left\| w \cdot \left(F^H D F \chi_1 - \phi \right) \right\|_1 + \lambda_1^{L_1} \left\| \nabla \chi_1 \right\|_1 \tag{A.1}$$

Using ADMM, we introduced an auxiliary variable $z_1 = \nabla \chi_1$, and decoupled the equation system, leading to the following augmented Lagrangian functional:

$$\arg\min_{\chi_1,\, z_1} \left\| w \cdot \left(F^H D F \chi_1 - \phi \right) \right\|_1 + \lambda_1^{L_1} \left\| z_1 \right\|_1 + \frac{\mu_1^{L_1}}{2} \left\| \nabla \chi_1 - z_1 + s_1 \right\|_2^2 \tag{A.2}$$

where s_1 is an Lagrange multiplier and $\mu_1^{L_1} > 0$ is a penalty parameter, in this case called gradient consistency weight. To decouple the χ_1 subproblem we introduced $z_2 = F^H D F \chi_1 - \phi$:

$$\arg\min_{\chi_1,\, z_1,\, z_2} \left\| w \cdot z_2 \right\|_1 + \lambda_1^{L_1} \left\| z_1 \right\|_1 + \frac{\mu_1^{L_1}}{2} \left\| \nabla \chi_1 - z_1 + s_1 \right\|_2^2 + \frac{\mu_2^{L_1}}{2} \left\| F^H D F \chi_1 - \phi - z_2 + s_2 \right\|_2^2 \tag{A.3}$$

where s_2 is an Lagrange multiplier and $\mu_2^{L_1} > 0$ is called data fidelity consistency weight.

We solved the χ_1 subproblem, the gradient operator can be decomposed as $\nabla = F^H E F$, where E is a diagonal matrix that represents the differential operation in frequency domain:

$$\arg\min_{\chi_1} \frac{\mu_1^{L_1}}{2} \left\| F^H E F \chi_1 - z_1 + s_1 \right\|_2^2 + \frac{\mu_2^{L_1}}{2} \left\| F^H D F \chi_1 - \phi - z_2 + s_2 \right\|_2^2 \tag{A.4}$$

$$\frac{\partial}{\partial \chi_1} \left(\frac{\mu_1^{L_1}}{2} \left\| F^H E F \chi_1 - z_1 + s_1 \right\|_2^2 + \frac{\mu_2^{L_1}}{2} \left\| F^H D F \chi_1 - \phi - z_2 + s_2 \right\|_2^2 \right) = 0 \tag{A.5}$$

$$\mu_1^{L_1} F^H E^H F \left(F^H E F \chi_1 - z_1 + s_1 \right) + \mu_2^{L_1} F^H D^H F \left(F^H D F \chi_1 - \phi - z_2 + s_2 \right) = 0 \tag{A.6}$$

$$\boxed{\chi_1 = F^H \frac{\mu_1^{L_1} E^H F \left(z_1 - s_1 \right) + \mu_2^{L_1} D^H F \left(z_2 - s_2 + \phi \right)}{\mu_1^{L_1} E^H E + \mu_2^{L_1} D^H D}} \tag{A.7}$$

We solved the z_1 subproblem by the soft thresholding operation:

$$\arg\min_{z_1} \lambda_1^{L_1} \left\| z_1 \right\|_1 + \frac{\mu_1^{L_1}}{2} \left\| \nabla \chi_1 - z_1 + s_1 \right\|_2^2 \tag{A.8}$$

$$\frac{\partial}{\partial z_1} \left(\lambda_1^{L_1} \left\| z_1 \right\|_1 + \frac{\mu_1^{L_1}}{2} \left\| \nabla \chi_1 - z_1 + s_1 \right\|_2^2 \right) = 0 \tag{A.9}$$

$$\lambda_1^{L_1} \text{sign}\left(z_1 \right) - \mu_1^{L_1} \left(\nabla \chi_1 - z_1 + s_1 \right) = 0 \tag{A.10}$$

In the optimal $z_1 = \left(\nabla \chi_1 + s_1 \right) - \frac{\lambda_1^{L_1}}{\mu_1^{L_1}} \text{sign}\left(z_1 \right)$. If $z_1 < 0 \implies \left(\nabla \chi_1 + s_1 \right) < \frac{\lambda_1^{L_1}}{\mu_1^{L_1}} \text{sign}\left(z_1 \right)$ and equivalently if $z_1 > 0 \implies \left(\nabla \chi_1 + s_1 \right) > \frac{\lambda_1^{L_1}}{\mu_1^{L_1}} \text{sign}\left(z_1 \right)$. Thus $\left| \nabla \chi_1 + s_1 \right| > \frac{\lambda_1^{L_1}}{\mu_1^{L_1}} \implies \text{sign}\left(\nabla \chi_1 + s_1 \right) = \text{sign}\left(z_1 \right)$. Then:

$$z_1 = \left(\nabla \chi_1 + s_1 \right) - \frac{\lambda_1^{L_1}}{\mu_1^{L_1}} \text{sign}\left(\nabla \chi_1 + s_1 \right)$$

In the case $z_1 = 0 \implies \text{sign}\left(\nabla \chi_1 + s_1 \right) \in [-1,\, 1]$ the optimal condition is: $0 = \left(\nabla \chi_1 + s_1 \right) - \frac{\lambda_1^{L_1}}{\mu_1^{L_1}} \text{sign}\left(\nabla \chi_1 + s_1 \right) \iff \left(\nabla \chi_1 + s_1 \right) \in \left[-\frac{\lambda_1^{L_1}}{\mu_1^{L_1}},\, \frac{\lambda_1^{L_1}}{\mu_1^{L_1}} \right] \iff \left| \nabla \chi_1 + s_1 \right| \leq \left| \frac{\lambda_1^{L_1}}{\mu_1^{L_1}} \right|$. Thus

$$\boxed{z_1 = \max\left(\left| \nabla \chi_1 + s_1 \right| - \frac{\lambda_1^{L_1}}{\mu_1^{L_1}},\, 0 \right) \cdot \text{sign}\left(\nabla \chi_1 + s_1 \right)} \tag{A.11}$$

We solved the z_2 subproblem by the soft thresholding operation as well:

$$\arg\min_{z_2} \|w \cdot z_2\|_1 + \frac{\mu_2^{L_1}}{2} \left\|F^H DF\chi_1 - \phi - z_2 + s_2\right\|_2^2 \tag{A.12}$$

$$\boxed{z_2 = \max\left(\left|F^H DF\chi_1 - \phi + s_2\right| - \frac{w}{\mu_2^{L_1}}, 0\right) \cdot \text{sign}\left(F^H DF\chi_1 - \phi + s_2\right)} \tag{A.13}$$

The update rules for the Lagrangian multipliers are given by:

$$s_1 = s_1 + F^H EF\chi_1 - z_1 \tag{A.14}$$

$$s_2 = s_2 + F^H DF\chi_1 - \phi - z_2 \tag{A.15}$$

A.2. ADMM Solver for Stage 2

The second stage of HD-QSM is to solve the following linear QSM functional with L2-norm:

$$\arg\min_{\chi_2} \frac{1}{2} \left\|\mathbb{W} \cdot \left(F^H DF\chi_2 - \phi\right)\right\|_2^2 + \lambda_1^{L_2} \|\nabla\chi_2\|_1 \tag{A.16}$$

where

$$\mathbb{W} = w \cdot \left(1 - \frac{\left|\phi - F^H DF\chi_1\right|}{\max\left(\left|\phi - \mathcal{F}^{\mathcal{H}}\mathcal{D}\mathcal{F}\chi_\infty\right|\right)}\right) \tag{A.17}$$

Using ADMM, we introduced an auxiliary variable $z_1 = \nabla\chi_2$, and decoupled the equation system, leading to the following augmented Lagrangian functional:

$$\arg\min_{\chi_2, z_1} \frac{1}{2} \left\|\mathbb{W} \cdot \left(F^H DF\chi_2 - \phi\right)\right\|_2^2 + \lambda_1^{L_2} \|z_1\|_1 + \frac{\mu_1^{L_2}}{2} \|\nabla\chi_2 - z_1 + s_1\|_2^2 \tag{A.18}$$

To decouple the χ_2 subproblem we introduced $z_2 = F^H DF\chi_2 - \phi$:

$$\arg\min_{\chi_2,\, z_1,\, z_2} \|\mathbb{W}\cdot z_2\|_2^2+\lambda_1^{L_2}\|z_1\|_1+\frac{\mu_1^{L_2}}{2}\|\nabla\chi_2-z_1+s_1\|_2^2+\frac{\mu_2^{L_2}}{2}\left\|F^H DF\chi_2-\phi-z_2+s_2\right\|_2^2 \tag{A.19}$$

We solved the χ_2 subproblem by closed form:

$$\arg\min_{\chi_2} \frac{\mu_1^{L_2}}{2}\left\|F^H EF\chi_2-z_1+s_1\right\|_2^2+\frac{\mu_2^{L_2}}{2}\left\|F^H DF\chi_2-\phi-z_2+s_2\right\|_2^2 \tag{A.20}$$

$$\frac{\partial}{\partial\chi_1}\left(\frac{\mu_1^{L_2}}{2}\left\|F^H EF\chi_2-z_1+s_1\right\|_2^2+\frac{\mu_2^{L_2}}{2}\left\|F^H DF\chi_2-\phi-z_2+s_2\right\|_2^2\right)=0 \tag{A.21}$$

$$\mu_1^{L_2}F^H E^H F\left(F^H EF\chi_2-z_1+s_1\right)+\mu_2^{L_2}F^H D^H F\left(F^H DF\chi_2-\phi-z_2+s_2\right)=0 \tag{A.22}$$

$$\boxed{\chi_2=F^H\frac{\mu_1^{L_2}E^H F\left(z_1-s_1\right)+\mu_2^{L_2}D^H F\left(z_2-s_2+\phi\right)}{\mu_1^{L_2}E^H E+\mu_2^{L_2}D^H D}} \tag{A.23}$$

We solved the z_1 subproblem by the soft thresholding operation:

$$\arg\min_{z_1}\lambda_1^{L_2}\|z_1\|_1+\frac{\mu_1^{L_2}}{2}\|\nabla\chi_2-z_1+s_1\|_2^2 \tag{A.24}$$

$$\boxed{z_1=\max\left(\left|\nabla\chi_2+s_1\right|-\frac{\lambda_1^{L_2}}{\mu_1^{L_2}},\,0\right)\cdot\operatorname{sign}\left(\nabla\chi_2+s_1\right)} \tag{A.25}$$

We solved the z_2 subproblem by the soft thresholding operation as well:

$$\arg\min_{z_2}\|\mathbb{W}\cdot z_2\|_2^2+\frac{\mu_2^{L_2}}{2}\left\|F^H DF\chi_2-\phi-z_2+s_2\right\|_2^2 \tag{A.26}$$

$$\boxed{z_2=\max\left(\left|F^H DF\chi_2-\phi+s_2\right|-\frac{\mathbb{W}}{\mu_2^{L_2}},\,0\right)\cdot\operatorname{sign}\left(F^H DF\chi_2-\phi+s_2\right)} \tag{A.27}$$

The update rules for the Lagrangian multipliers are given by:

$$s_1 = s_1 + F^H E F \chi_2 - z_1 \tag{A.28}$$

$$s_2 = s_2 + F^H D F \chi_2 - \phi - z_2 \tag{A.29}$$

A.3. Challenge 2.0 Experiment

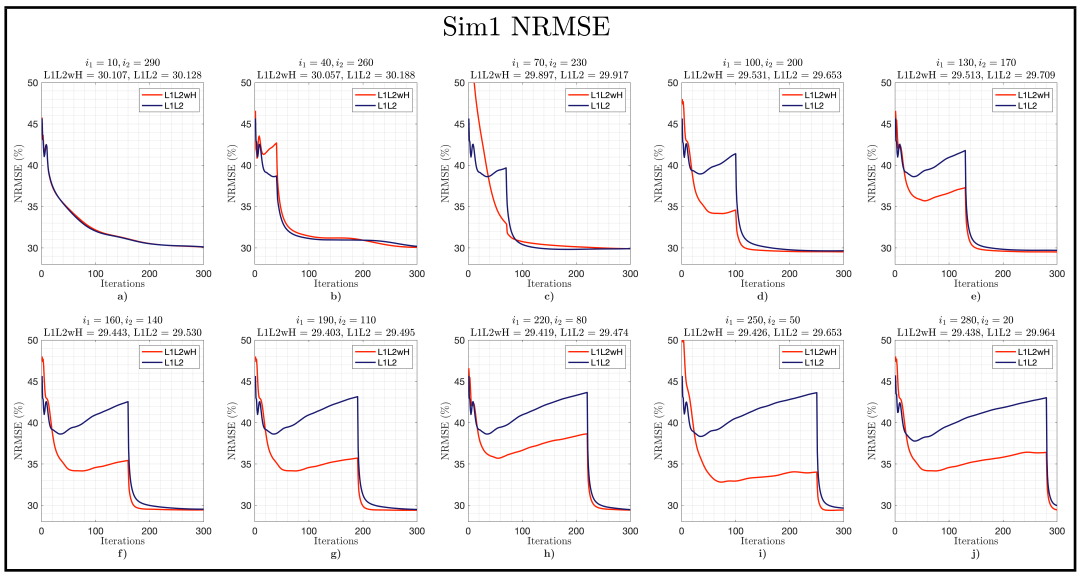

FIGURE A.1. NRMSE evolution of Sim1 optimal reconstructions for different i_1. The error difference obtained between the free parameter method and the proposed heuristic is less than 1% for all i_1. The difference between the best and the worst reconstruction is less than 1%, indicating that the number of iterations of L1 norm is not an extremely determinant factor, which confirms the hypothesis that the stage of an L1 norm solution is a better starting point than 0.

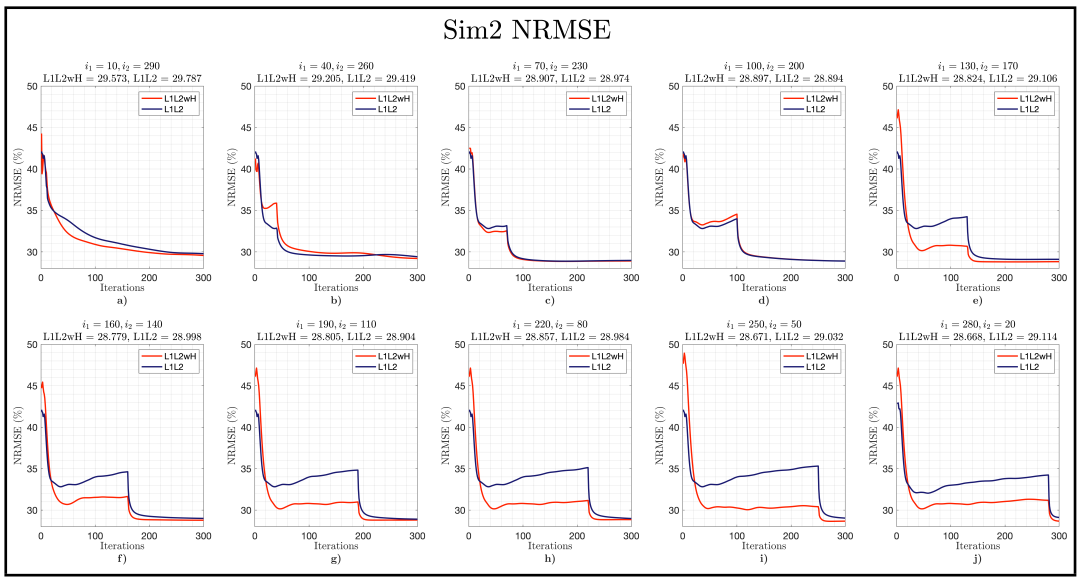

FIGURE A.2. NRMSE evolution of Sim2 optimal reconstructions for different i_1.

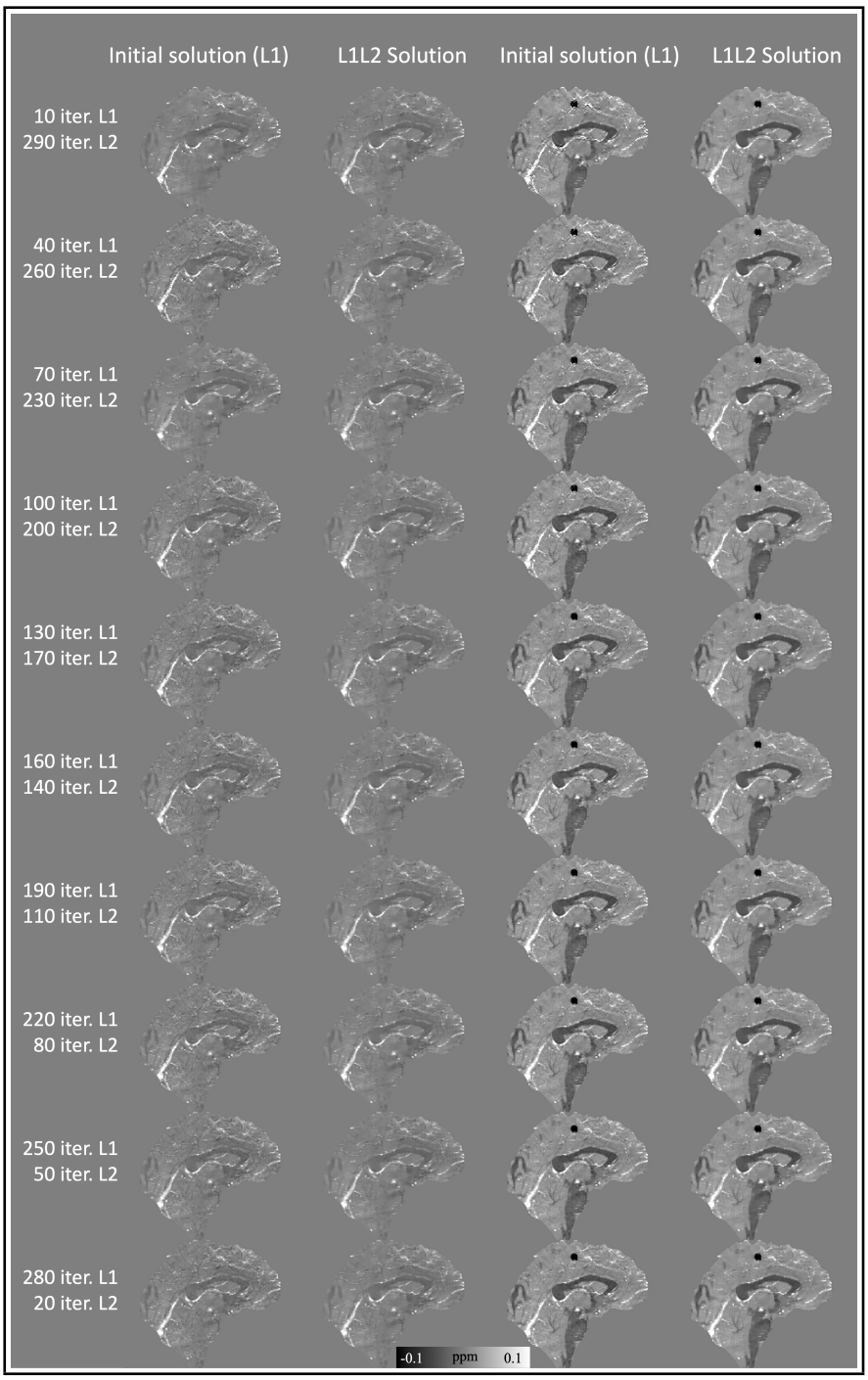

FIGURE A.3. Solutions at the end of stage 1 and stage 2 for Sim1 and Sim2. The solutions at the end of stage 1 show a noisy appearance with streaking artifacts (see around the calcification), but with good structural definition. The final solutions maintain the structural details but do not show the noise and streaking artifacts.

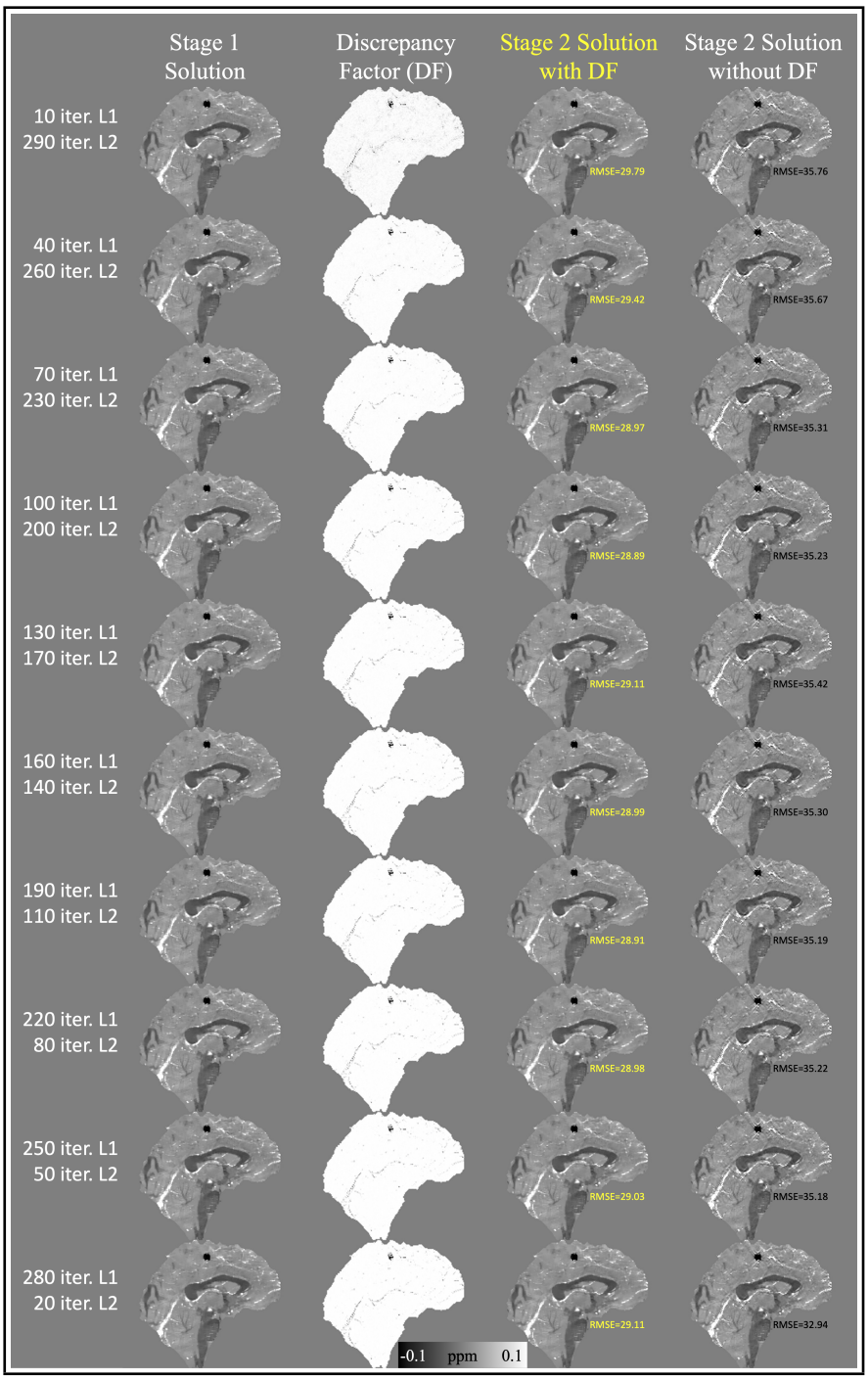

FIGURE A.4. The first column presents the solution at the end of stage 1, the second the discrepancy factor which weights the data consistency weight, the third the solution of stage 2 using the adjustment factor and the fourth the solution without using the adjustment factor with the same parameters.

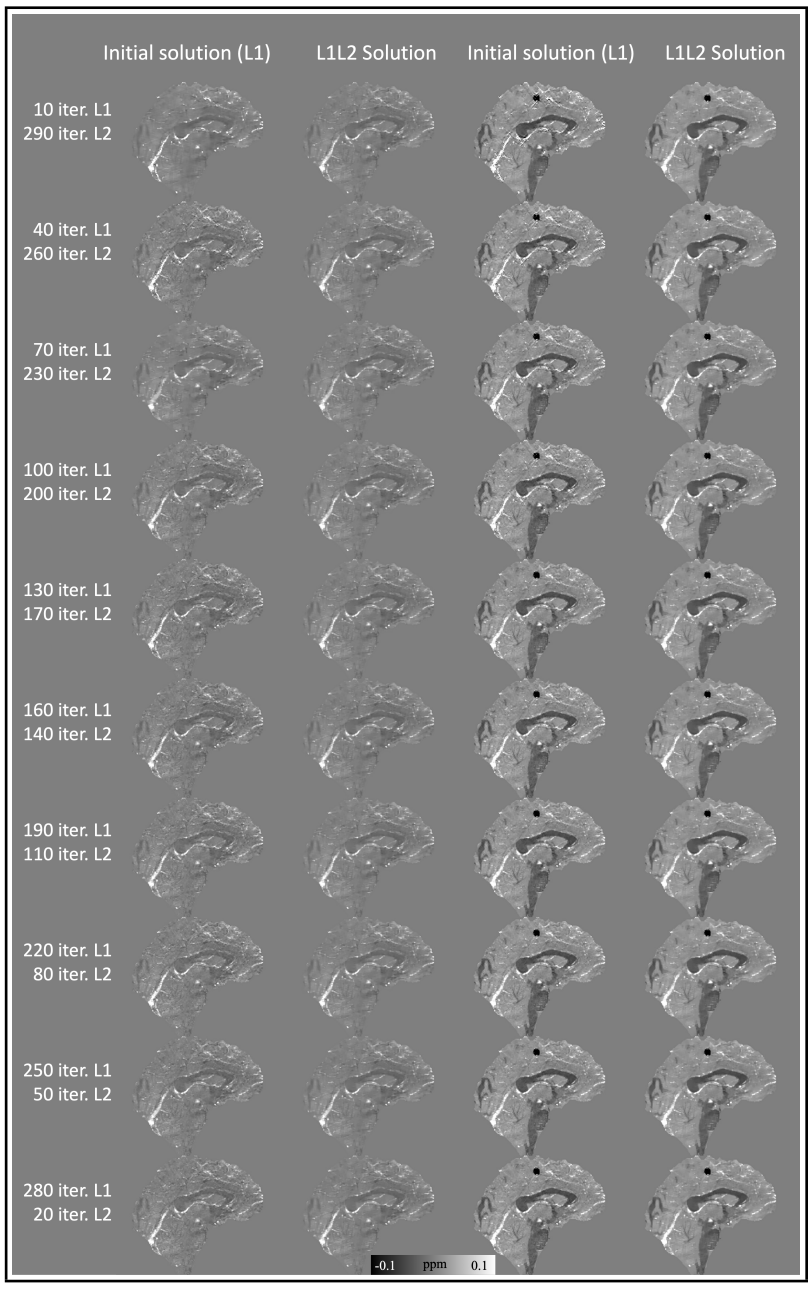

FIGURE A.5. NRMSE optimized solutions of HD-QSM without the discrepancy factor. The first column presents the solution at the end of stage 1 and the second column the final solution.

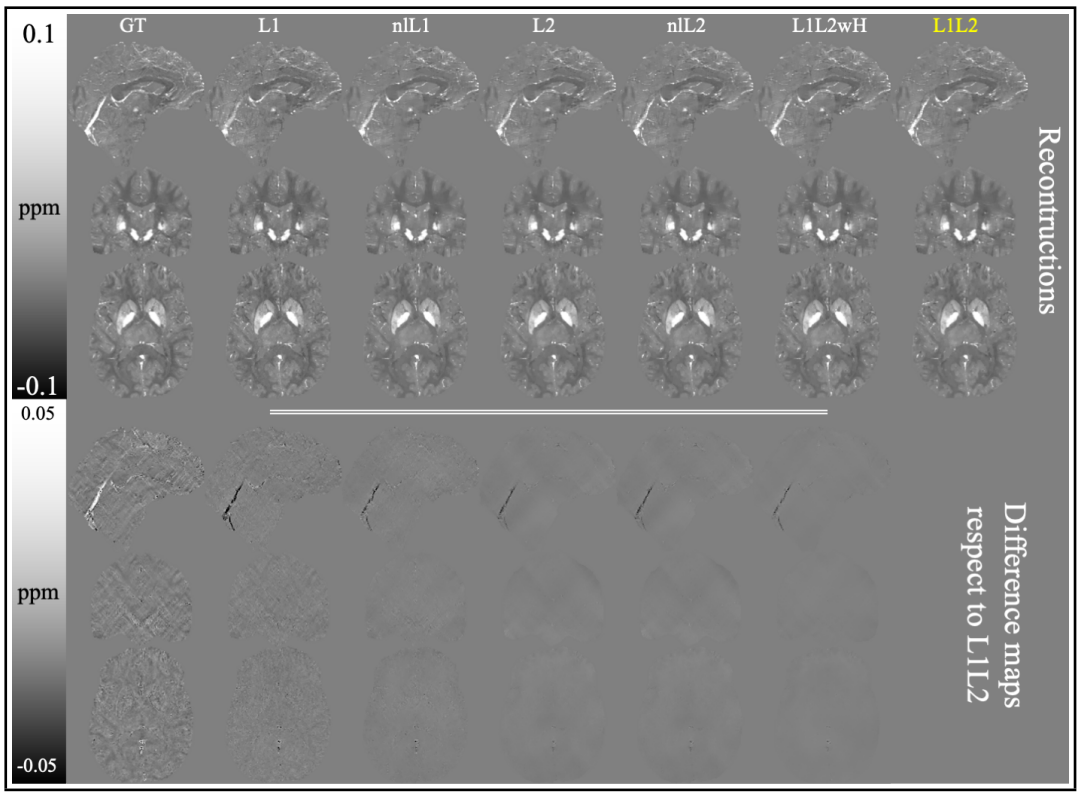

FIGURE A.6. Optimal NRMSE reconstructions of Sim 1. For the search of the optimum of L1L2wH a search was performed in a vector space of 5x5x5x5 $(\lambda_1^{L_1}, \mu_1^{L_1}, \lambda_1^{L_2}, \mu_1^{L_2})$, once the optimum of this space was located, a second search was performed in a space of the same size in the vicinity of the optimum, In total 3 search processes were performed for each simulation, which is 3750 reconstructions, while for L1L2 only 50 reconstructions were necessary.

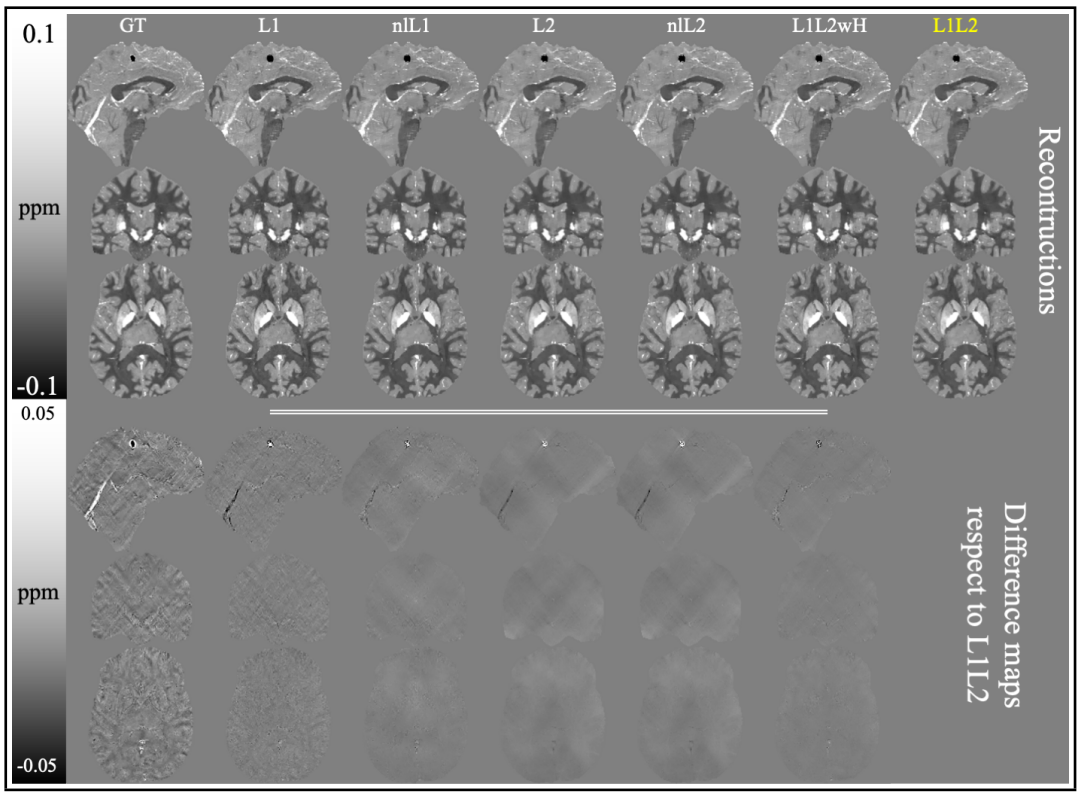

FIGURE A.7. Optimal NRMSE reconstructions of Sim 2. For the search of the optimum of L1L2wH a search was performed in a vector space of 5x5x5x5 $(\lambda_1^{L_1}, \mu_1^{L_1}, \lambda_1^{L_2}, \mu_1^{L_2})$, once the optimum of this space was located, a second search was performed in a space of the same size in the vicinity of the optimum, In total 3 search processes were performed for each simulation, which is 3750 reconstructions, while for L1L2 only 50 reconstructions were necessary.

APPENDIX B. NON-REGULARIZED DIPOLE INVERSION WITH STREAKING SUPPRESSION VIA L1-NORM OPTIMIZATION

B.1. Title and authors

Non-regularized Dipole Inversion with streaking suppression via L1-norm optimization. Poster at ISMRM21. The authors are: Mathias Lambert, Cristián Tejos, Carlos Milovic.

B.2. Synopsis

Non-regularized QSM reconstructions are feasible by stopping gradient descent methods before they diverge. These methods consume less computation time, while avoiding the time required for parameter selection. In this work we present a linear dipole inversion method without regularization that uses the L1-norm in a proximal step to prevent streaking propagation and present more robustness against phase outliers. Compared to the Nonlinear Dipole Inversion method, our implementation achieved lower RMSE scores in phantom experiments and in vivo reconstructions with fewer artifacts.

B.3. Abstract

B.3.1. Introduction

Quantitative susceptibility mapping is typically performed by optimization methods that minimize a functional that consists of regularization and data fidelity terms. These methods require fine-tuning the parameters associated with the regularization terms. Recently, a non-linear inversion method (Nonlinear Dipole Inversion, NDI) (Polak et al., 2020) was presented with comparable in vivo results with state-of-the-art methods such as MEDI (Liu et al., 2013) and FANSI (Milovic et al., 2018). It is possible to optimally use NDI without a regularizer, by early stopping the algorithm (before it diverges). Nevertheless, NDI is prone to noise amplification, and is susceptible to strong streaking artifacts. L1-norm data fidelity terms have been successfully used in conjunction with the Total Variation regularization (Milovic, Lambert, et al., 2021) to suppress the appearance of streaking

artifacts in QSM. Here, we present a robust and fast non-regularized linear method that uses a L1-norm data fidelity term to prevent streaking artifact propagation.

B.3.2. Methods

We propose to solve the dipole inversion problem by formulating the QSM functional using a L1-norm (nDI-L1) data fidelity term (without regularization):

$$\arg\min_{\chi} \left\| w \cdot \left(F^H D F \chi - \phi \right) \right\|_1 \tag{B.1}$$

where F is the Fourier transform with its inverse F^H, D is the dipole kernel (Salomir et al., 2003; J. Marques & Bowtell, 2005), ϕ is the tissue phase, χ is the susceptibility distribution, w is a magnitude-based weight or ROI mask. To solve this functional we use the auxiliary variable $z = \left(F^H D F \chi - \phi \right)$ to augment the functional in a proximal framework:

$$\arg\min_{\chi,\, z} \left\| w \cdot z \right\|_1 + \frac{\lambda}{2} \left\| \left(F^H D F \chi - \phi \right) \right\|_2^2 \tag{B.2}$$

The solution scheme is to employ gradient descent for the χ sub-problem and a proximal step for z:

$$\chi_{k+1} = \chi_k - \tau \cdot F^H D^H F \left(\left(F^H D F \chi - \phi \right) - z \right) \tag{B.3}$$

$$z_{k+1} = \max\left(\left| F^H D F \chi_{k+1} - \phi \right| - \frac{w}{\lambda},\, 0 \right) \cdot \text{sign}\left(F^H D F \chi_{k+1} - \phi \right) \tag{B.4}$$

where τ is the gradient step size and λ is a Lagrangian weight that acts as the L1 proximal soft-thresholding parameter.

Instead of a fixed λ value, we λ iterative update λ to threshold a given percentage of the discrepancy between the input data and the proposed solution (cut-off ratio). The gradient step size (τ) is set to 2. As in the NDI algorithm, the number of iterations is the most critical parameter.

We compared the proposed method with NDI in the following experiments:

(i) COSMOS (Liu et al., 2009) forward simulations: From a COSMOS brain reconstruction (2016 QSM challenge dataset) (Langkammer et al., 2018) we synthesized the local phase and added complex noise to the complex image (SNR=100). In addition, two simulated lesions were added, one paramagnetic (-0.55 ppm) and one diamagnetic (0.3 ppm), to mimic highly noisy phase inconsistencies. We tested the performance of the reconstruction using $w = 1$, $w =$ mask and $w =$ magn as weighting methods.

(ii) SIM2SNR1: Using SIM2SNR1 dataset (2019 QSM challenge) (Committee et al., 2021; J. P. Marques et al., 2021) we compared the performance using the official metrics, plus HFEN (Ravishankar & Bresler, 2011) and XSIM (Milovic, Tejos, & Irarrazaval, 2019). We used the provided frequency map data and the masked magnitude data as weight. We zero-padded the field map to 256x256x256 voxels.

(iii) IN-VIVO: Phillips Ingenia 3T. TGE sequence, voxel size: 0.59x0.59x1mm, TR=44ms, TE=7.2ms, ΔTE=6.2ms, 5 echoes, bandwidth 550.5Hz. We perform Laplacian phase unwrapping (Li, Wu, & Liu, 2011) and background field removal using LBV (Zhou, Liu, Spincemaille, & Wang, 2014) and VSHARP (Li et al., 2011).

B.3.3. Results

Figure B.1 shows the results using the COSMOS-brain example. nDI-L1 achieved better RMSE scores and it is evident that nDI-L1 manages to effectively reduce streaking artifacts surrounding the lesions. The nDI-L1 reconstruction has a smoother appearance than NDI reconstruction, in which a better definition of the vein is observed. Figure B.2 shows the optimal (RMSE-based) reconstruction and metrics of the SIM2SNR1 dataset. It is observed that nDI-L1 reconstructs a smaller calcification than NDI, which is closer to the ground truth. Figure B.3 shows the results of the experiment with in-vivo data.

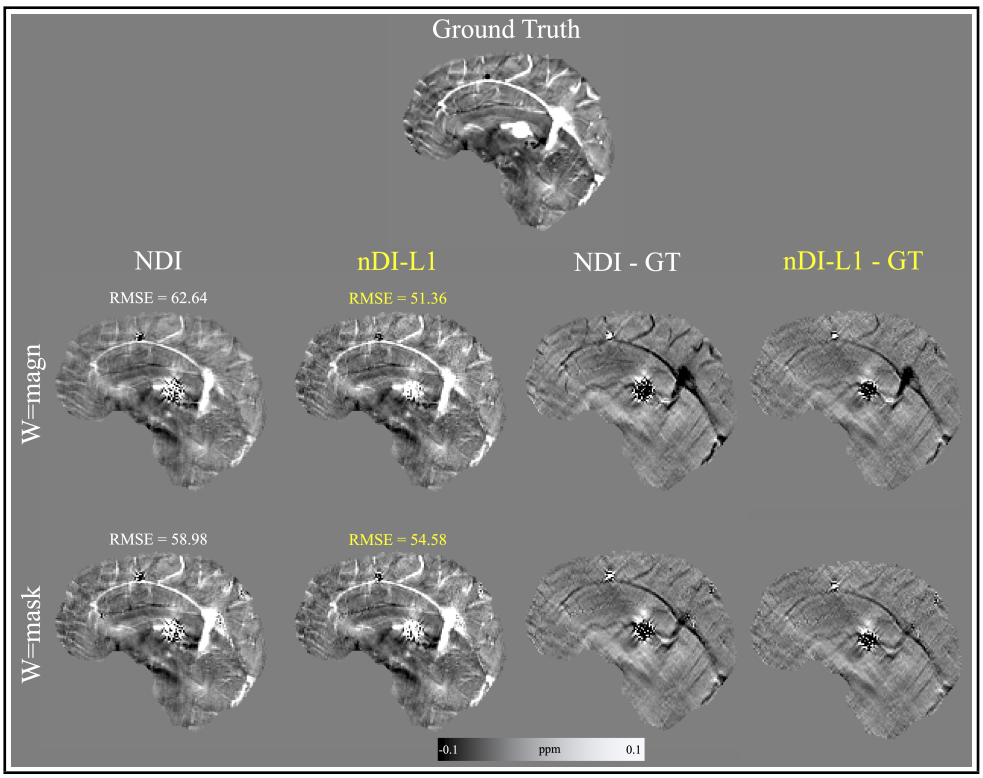

FIGURE B.1. Optimal (RMSE-based) reconstructions of the COSMOS forward simulation.

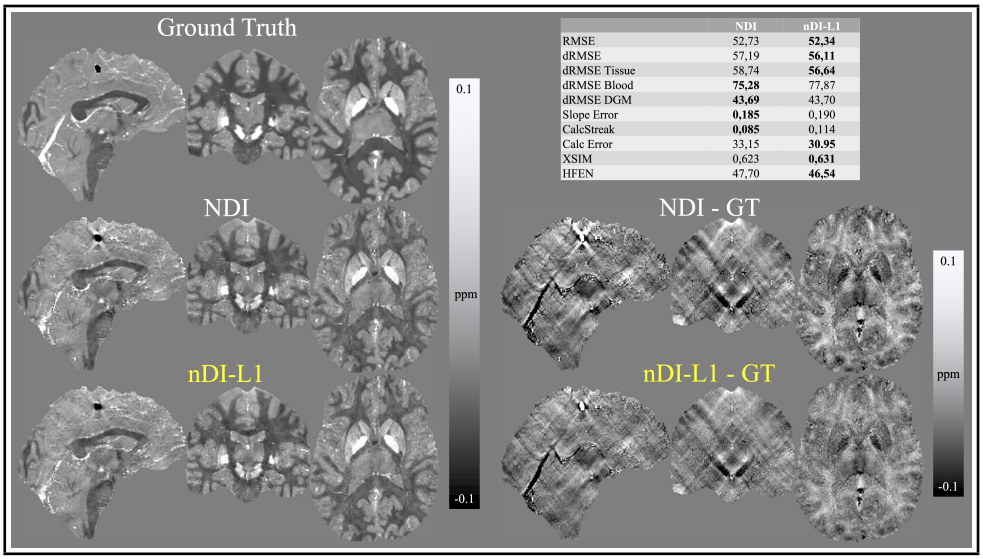

FIGURE B.2. Optimal (RMSE-based) reconstructions of the QSM Challenge 2.0 SIM2SNR1 dataset. The provided multi-echo data was used.

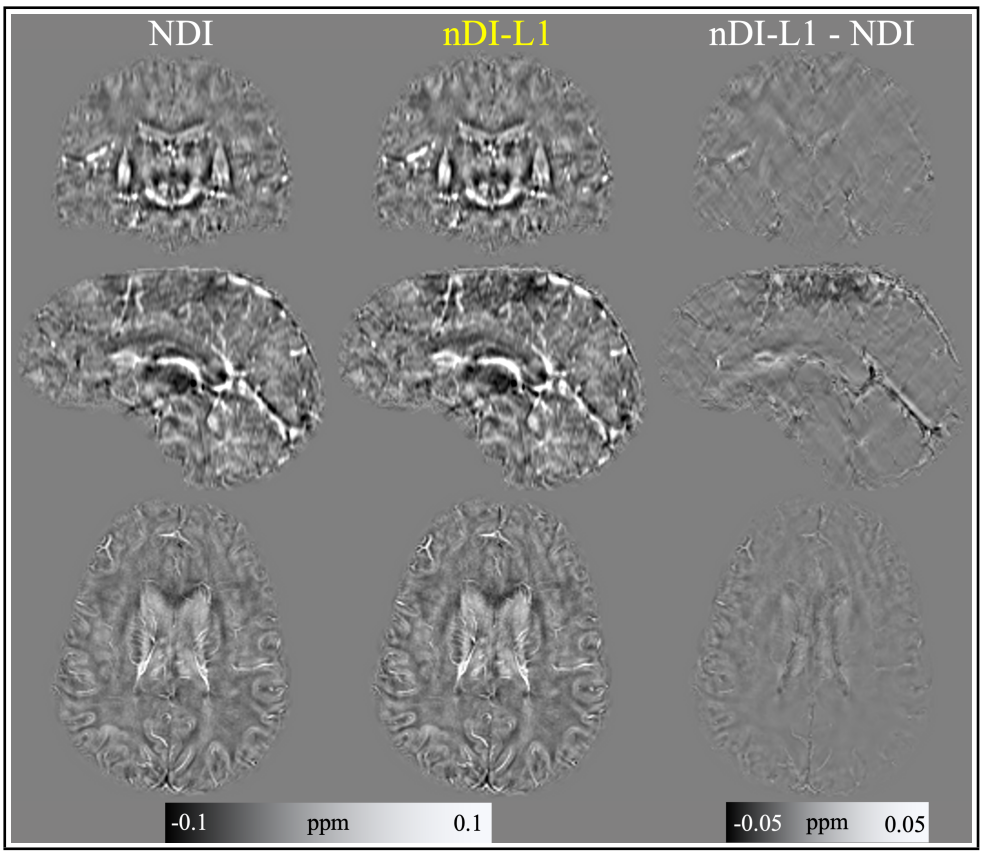

FIGURE B.3. Results in in-vivo data. The optimal number of iterations was selected by visually inspecting the result of each iteration.

B.3.4. Discussion & Conclusion

The proposed nDI-L1 method shows good performance in qualitative metrics in our experiments. Despite having a worse CalcStreak score than NDI, nDI-L1 more effectively suppressed the streaks and achieved a more accurate representation of the calcification (CalcError metric). This might suggest a limitation in the CalcStreak metric. The use of the L1-norm makes non-regularized methods based on gradient descent solvers robust to the generation of streaking artifacts and to noise. nDI-L1 has the quality of performing quick reconstructions saving us the work of fine-tuning regularization parameters, which usually requires multiple reconstructions, which costs a lot of time.

B.3.5. Acknowledgements

This work has been funded by projects Fondecyt 1191710, PIA-ACT192064, and the Millennium Nucleus on Cardiovascular Magnetic Resonance of the Millennium Science Initiative NCN17_129, by the National Agency for Research and Development, ANID. Dr Carlos Milovic is supported by Cancer Research UK Multidisciplinary Award C53545/A24348.

APPENDIX C. IMPROVING QUANTITATIVE SUSCEPTIBILITY MAPPING RECONSTRUCTIONS VIA NON-LINEAR HUBER LOSS DATA FIDELITY TERM (HUBER-QSM)

C.1. Title and authors

Improving Quantitative Susceptibility Mapping reconstructions via non-linear Huber loss data fidelity term (Huber-QSM). Poster at ISMRM21. The authors are: Mathias Lambert, Carlos Milovic, Cristián Tejos.

C.2. Synopsis

Compared to L2-norm based QSM reconstructions, methods based on L1-norm data consistency are less prone to artifact generation caused by phase inconsistencies (e.g. unwrapping artifacts, intravoxel dephasing). However, L2-norm methods present better denoising performance in high SNR regions. Here, we present a QSM algorithm that combines the strengths of the L1- and L2-norms, using Huber's loss function as the data consistency term. Simulations and in vivo reconstructions showed enhanced performance, with superior artifact suppression capabilities of our proposed method.

C.3. Abstract

C.3.1. Introduction

Susceptibility maps are estimated by solving an ill-posed inverse problem. The source-to-field problem is modeled by a magnetic dipole convolution. The magnetic dipole kernel has a zero-valued bi-conical surface in the frequency space (Salomir et al., 2003; J. Marques & Bowtell, 2005). This singularity makes the noise propagate through the reconstructed maps generating the so-called streaking artifacts (Shmueli et al., 2009). QSM reconstruction algorithms with data consistencies based the L1-norm probed to be more robust against phase outliers than those using the L2-norm, preventing the generation of artifacts (Milovic,

Lambert, et al., 2021). However, L2-norm based methods have shown better noise management on high SNR regions. In this thesis we present a new data consistency term that combines the L1- and L2-norms by using the Huber loss (Huber, 1964).

C.3.2. Methods

The proposed method consist in solving the following nonlinear functional (Liu et al., 2013; Milovic et al., 2018):

$$\arg\min_{\chi} h_{\delta}\left(w \cdot \left(e^{iF^{H}DF\chi} - e^{i\phi}\right)\right) + \lambda \cdot \mathrm{TV}\left(\chi\right) \tag{C.1}$$

where F is the Fourier transform with its inverse F^{H} , D is the dipole kernel, ϕ is the tissue phase, χ is the susceptibility distribution, w is a magnitude-based weight or ROI binary mask, TV$(\cdot)$ is the total variation regularizer (Chen & Cheng, 2012), and λ is the regularization weight. $h_{\delta}\left(\cdot\right)$ is the Huber loss defined by:

$$h_{\delta}\left(x\right) = \begin{cases} \frac{1}{2\cdot\delta}x^{2} & |x| \leq \delta \\ |x| - \frac{\delta}{2} & |x| > \delta \end{cases} \tag{C.2}$$

where $\delta > 0$ is the threshold parameter. We solve this optimization problem using the ADMM framework (Bilgic et al., 2015). To decouple the data fidelity term, we add the following auxiliary variables $z_1 = F^{H}DF\chi$ and $z_2 = e^{iz_1} - e^{i\phi}$. The z_1 subproblem is solved as shown earlier for the L1-norm (Milovic et al., 2018; Milovic, Lambert, et al., 2021), with a Newton-Raphson iterative approach. The solution of the z_2 subproblem is given by the following shrinkage function:

$$z_2 = \frac{\delta \cdot \mu_2 \cdot \left(e^{iz_1} - e^{i\phi} + s_2\right) + w^2 \cdot \max\left(\left|e^{iz_1} - e^{i\phi} + s_2\right| - \frac{w^2+\mu_2\cdot\delta}{w\cdot\mu_2},\, 0\right) \cdot \mathrm{sign}\left(e^{iz_1} - e^{i\phi} + s_2\right)}{w^2 + \delta \cdot \mu_2} \tag{C.3}$$

Figure C.1 shows the cost and shrinkage functions of $h_{\delta}\left(\cdot\right)$, L1-norm and L2-norm.

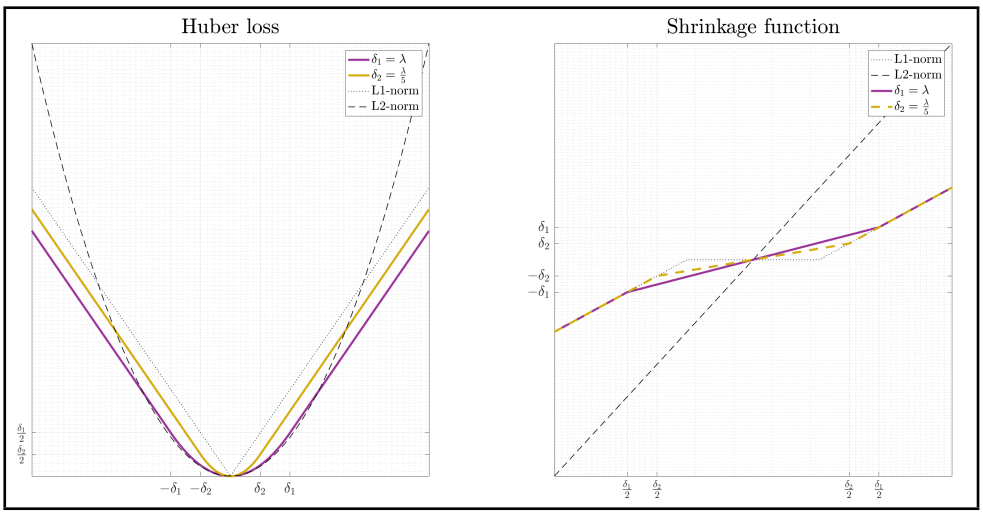

FIGURE C.1. The graph on the left shows the cost functions, you can see how the Huber loss penalizes less the large values. The graph on the right shows the penalty functions, you can see that as the parameter δ decreases the Huber loss converges to a soft threshold(L1-norm).

We compared the proposed method (nlHu) with non-linear L2-norm (FANSI) (Milovic et al., 2018) and non-linear L1-norm (nlL1) (Milovic, Lambert, et al., 2021) methods, all with total variation regularization, in the following experiments:

(i) COSMOS forward simulations: From a COSMOS (Liu et al., 2009) brain reconstruction (2016 QSM challenge dataset) (Langkammer et al., 2018) we synthesized the local phase and added complex noise to the complex image (SNR=40 and SNR=100). In addition, two simulated lesions were added, one paramagnetic (-0.5 ppm) and one diamagnetic (0.2 ppm), to mimic highly noisy phase inconsistencies.

(ii) SIM2SNR1: Using the SIM2SNR1 dataset (2019 QSM challenge) (Committee et al., 2021; J. P. Marques et al., 2021) we compared the performance using the official metrics, plus HFEN (Ravishankar & Bresler, 2011) and XSIM (Milovic, Tejos, & Irarrazaval, 2019). We used multi-echo data and masked magnitude-based weight. For the inversions we used a zero-padding to form a volume of 256x256x256 voxels.

(iii) IN-VIVO Data: Siemens 3T scanner (Magnetom Trio Tim; Siemens Healthcare, Erlangen, Germany) with a 12-channel phased-array head coil. GRE sequence with 6 echoes. A patient showing extensive bleeding was scanned with the following sequence parameters: TE1=4.92ms, ΔTE=4.92ms, TR=35ms, flip angle=15°, 232×288×64 matrix with 0.8×0.8×2mm3 voxels, and Tacq=4:51min. We performed Laplacian phase unwrapping (Li et al., 2011) and background field removal using PDF (Liu et al., 2011) and VSHARP (Li et al., 2011).

C.3.3. Results

Figure C.2 presents the COSMOS-based reconstructions for both SNR levels, at both noise levels nlHu obtained the lowest RMSE. Figure C.3 presents the sagittal slices of reconstructions of SNR=100 with the simulated lesions. SIM2SNR1 reconstructions are presented in Figure C.4, along with difference maps and a table with the performance metrics. In-vivo reconstructions and difference maps are shown in Figure C.5.

C.3.4. Discussion & Conclusion

In Figure C.2, we can see that in comparison to FANSI, nlHu manages to reconstruct the veins in the cortical zone more effectively. In the same figure we can see that nL1 reconstructions have a noisier appearance than nlHu. In Figure C.3 we can see that nlHu manages to stop the propagation of streaking artifacts. The metrics obtained in experiment 2 show that nlHu has better performance than FANSI and similar performance to nlL1. However, the results of the other experiments show that nlHu has a better performance than nlL1 in areas with high SNR. Although nlHu has one additional parameter over FANSI, optimizing it does not require much effort. Our simulated experiments revealed a convex behavior of δ on the RMSE, whereas it is possible to fine-tune the regularization parameter (λ) first and then δ. The experiments we conducted show the importance of the term data consistency in noise reduction. The Huber loss combines the strengths of the L1- and L2-norms into a single term.

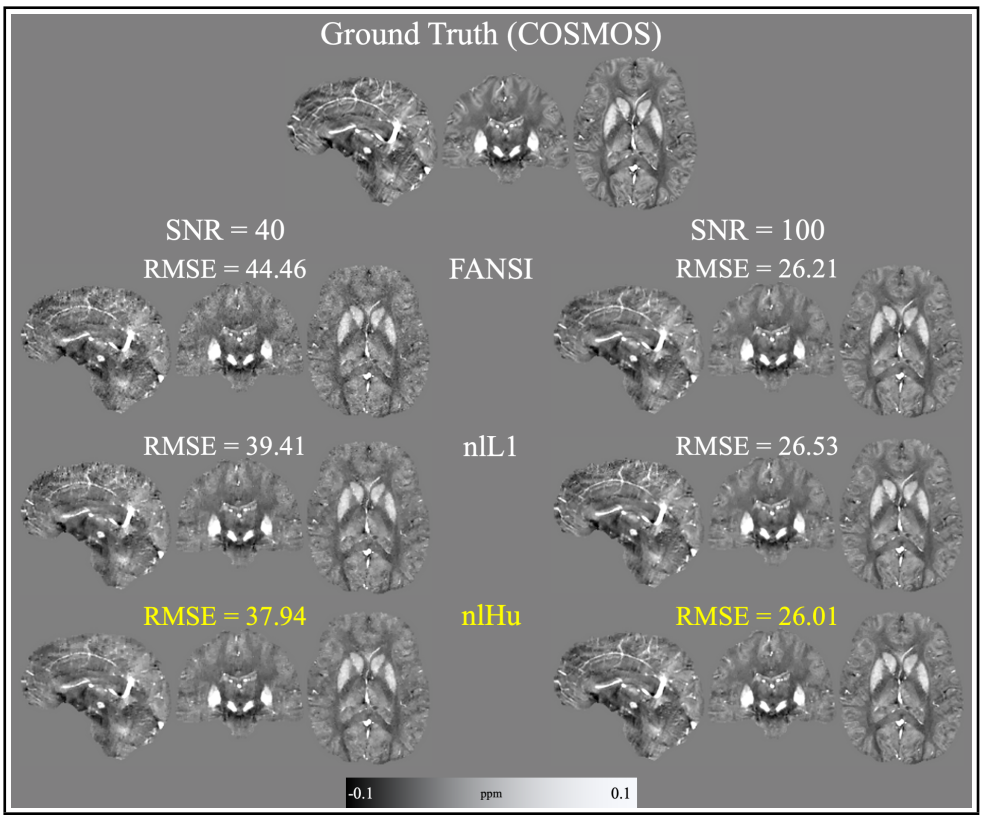

FIGURE C.2. COSMOS forward simulation results. 500 iterations were performed on all reconstruction methods. In the results with snr = 40, it is observed that the Huber loss has a better noise reduction capacity than the L1- and L2-norms. In the results with snr = 100, it is observed that nlHu, unlike FANSI manages to reconstruct the veins in the cortical area and, unlike nlL1, it has a less noisy appearance

C.3.5. Acknowledgements

This work has been funded by projects Fondecyt 1191710, PIA-ACT192064, and the Millennium Nucleus on Cardiovascular Magnetic Resonance of the Millennium Science Initiative NCN17_129, by the National Agency for Research and Development, ANID. We thank Dr. Christian Langkammer from the Medical University of Graz, Austria, for sharing his data with us and for his support.

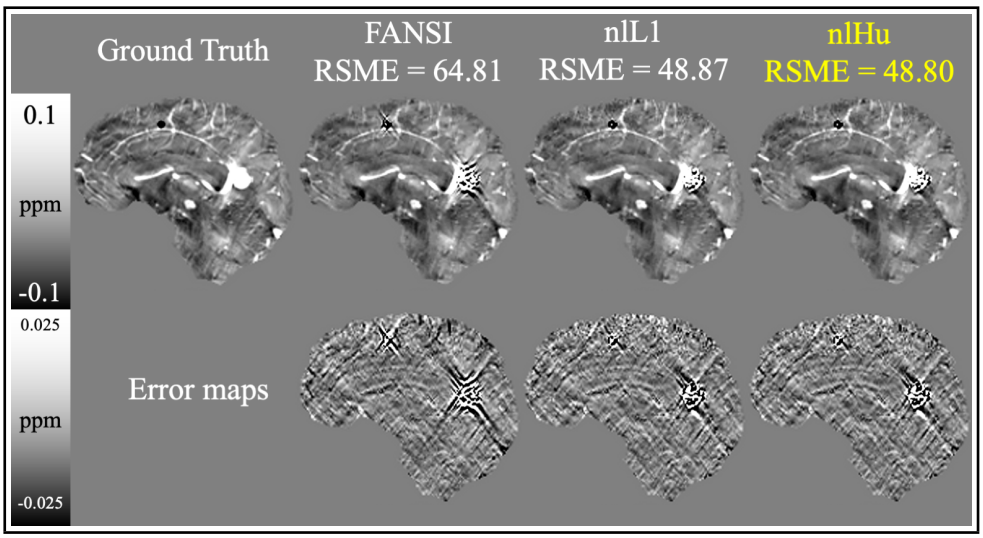

FIGURE C.3. COSMOS-based forward simulation reconstructions including two lesions simulating diamagnetic and paramagnetic tissues, and zero effective signal magnitude. Results are provided without masking of lesions. This tests the robustness against signal inconsistencies. 500 iterations were performed in each method.

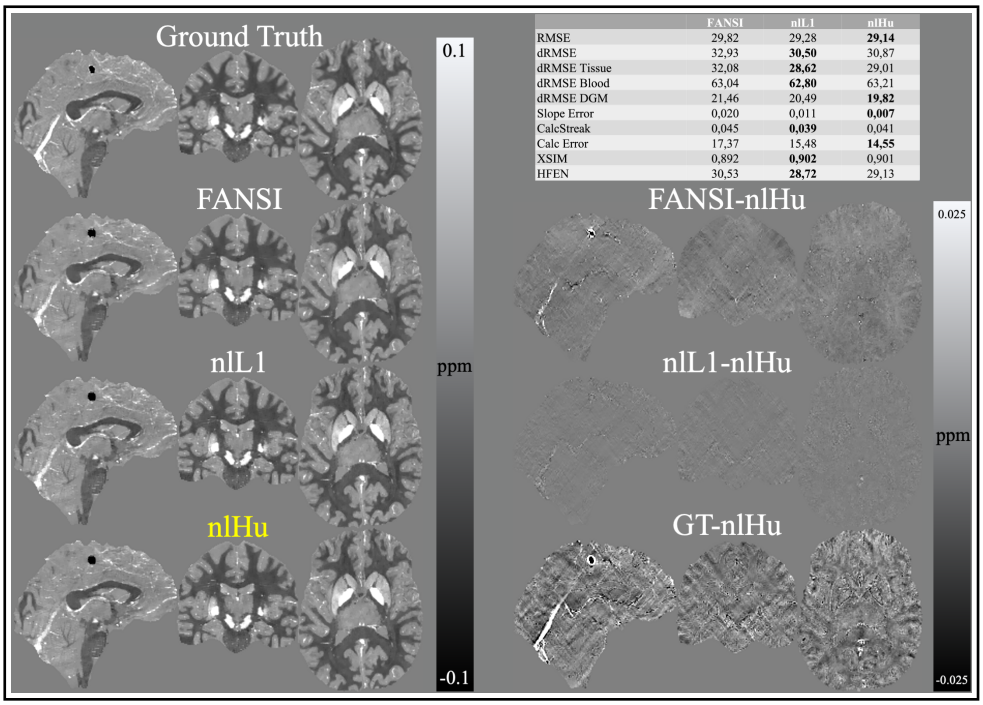

	FANSI	nlL1	nlHu
RMSE	29,82	29,28	**29,14**
dRMSE	32,93	**30,50**	30,87
dRMSE Tissue	32,08	**28,62**	29,01
dRMSE Blood	63,04	**62,80**	63,21
dRMSE DGM	21,46	20,49	**19,82**
Slope Error	0,020	0,011	**0,007**
CalcStreak	0,045	**0,039**	0,041
Calc Error	17,37	15,48	**14,55**
XSIM	0,892	**0,902**	0,901
HFEN	30,53	**28,72**	29,13

FIGURE C.4. Optimal (RMSE-based) reconstructions of the QSM Challenge 2.0 SIM2SNR1 dataset. The provided multi-echo data was used. 500 iterations were performed in each method.

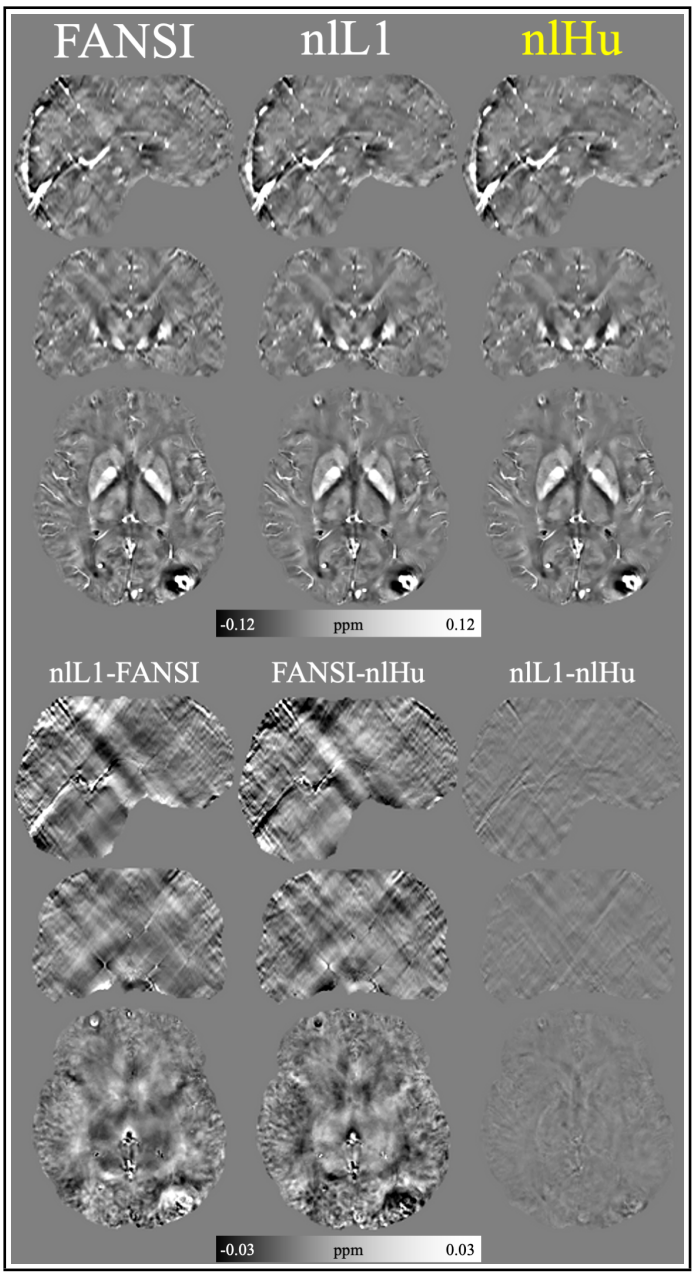

FIGURE C.5. Optimal (L-curve analysis) reconstructions of the in-vivo data. Difference maps between algorithms also provided. 500 iterations were performed in each method.

LIST OF PUBLICATIONS, CONFERENCES AND AWARDS

ISI Journals

1. **Lambert M**, Tejos C, Langkammer C, Milovic C. Hybrid data fidelity term approach for Quantitative Susceptibility Mapping. [Manuscript submitted to Magn. Reson. Med. for publication].
2. Milovic C, **Lambert M**, Langkammer C, Bredies K, Irarrazaval P, Tejos C. Streaking artifact suppression of quantitative susceptibility mapping reconstructions via L1-norm data fidelity optimization (L1-QSM). Magn Reson Med. 2021; 00: 1– 17. https:// doi.org/ 10.1002/ mrm.28957

International Conferences

1. **Lambert M**, Milovic C, Tejos C. Improving Quantitative Susceptibility Mapping reconstructions via non-linear Huber loss data fidelity term (Huber-QSM). *In:Proc.Intl. Soc. Mag. Reson. Med*, 2021;p3983.
2. **Lambert M**, Tejos C, Milovic C. Non-regularized Dipole Inversion with streaking suppression via L1-norm optimization. *In:Proc.Intl. Soc. Mag. Reson. Med*, 2021;p3984.
3. **Lambert M**, Milovic C, Tejos C. Hybrid Data fidelity term approach for Quantitative Susceptibility Mapping. *In:Proc.Intl. Soc. Mag. Reson. Med*, 2020;p3205.
4. Milovic C, **Lambert M**, Langkammer C, Bredies K, Tejos C, Irarrazaval P. QSM streaking suppression with L1 data fidelity terms. *In:Proc.Intl. Soc. Mag. Reson. Med*, 2020;p3257.

International Awards

1. **1st Place at the Lowest RMSE Category - QSM challenge 2.0**. 5th INTERNATIONAL WORKSHOP ON MRI PHASE CONTRAST & QUANTITATIVE SUSCEPTIBILITY MAPPING. Seoul, S.Korea. 2019.